Geochemical evolution of rodingites during subduction: insights from Cerro del Almirez (southern Spain)

Casto Laborda-López [a*], Claudio Marchesi [b,c], Vicente López Sánchez-Vizcaíno [a], María Teresa Gómez-Pugnaire [b,c], Christopher W. Dale [d], Antonio Jabaloy-Sánchez [e], José Alberto Padrón-Navarta [f], Manuel J. Román-Alpiste [c], Carlos J. Garrido [c]

(a) Departamento de Geología (Unidad Asociada al IACT-CSIC), Universidad de Jaén, Linares (Jaén), Spain
(b) Departamento de Mineralogía y Petrología, Universidad de Granada, Granada, Spain
(c) Instituto Andaluz de Ciencias de la Tierra, CSIC-Universidad de Granada, Armilla, Granada, Spain
(d) Department of Earth Sciences, Durham University, Durham DH1 3LE, United Kingdom
(e) Departamento de Geodinámica, Universidad de Granada, Granada, Spain
(f) Géosciences Montpellier, UMR 5243, CNRS-Université de Montpellier et Université des Antilles, Montpellier, France

Submitted to

Lithos

[*] Address of the corresponding author: Universidad de Jaén, Departamento de Geología, Campus Científico Tecnológico de Linares, Avda. de la Universidad s/n, 23700 Linares, Jaén, Spain. Tel.: 0034 953 648581. Fax: 0034 953 648622. Email: claborda@ujaen.es

ABSTRACT

Metarodingites from Cerro del Almirez (Betic Cordillera, southern Spain) experienced multiple mineralogical and compositional changes during their evolution, from rodingitization on the seafloor to dehydration of the hosting subducted antigorite serpentinites at ~ 1.7 GPa and 650 ºC. Basaltic and doleritic protoliths of Grandite-metarodingites lost alkaline metals (Na, K, Cs and Rb), Si, Ba, Pb and Sr, and gained Ca through intense seafloor rodingitization by highly reducing fluids reacting with serpentinites. Rare earth elements in whole-rocks, conversely, preserved their igneous abundances during rodingitization and partitioned into the new metamorphic assemblage dominated by granditic garnet, chlorite and diopside. At the ocean floor and during subduction, the strong gradients of chemical potentials of Mg, Ca and Al at the serpentinite-rodingite interface triggered the transformation of metarodingites to metasomatic chlorite-blackwalls and of host serpentinites to chlorite (± olivine)-diopside rims.

Grandite-metarodingites interacted during subduction with fluids released by the brucite breakdown in serpentinites at ~ 1.5 GPa, leading to oxidation of iron, precipitation of new andradite garnets with high MREE/HREE ratios, and loss of Re. Strong fluxing of fluids produced by the antigorite breakdown in serpentinites at ~ 1.7 GPa promoted the transformation of Grandite- to Epidote-metarodingites. This transformation caused the release of Ca and Mn into serpentinite-derived fluids and the incorporation of Si, Sr, Pb, Ba ± Eu into metarodingites, especially in epidote. Pyralspite-metarodingites formed at peak metamorphic conditions (~ 1.8 GPa and 680 ºC) by, among other reactions, epidote breakdown that liberated Ca, Sr and Pb into fluids. Finally, all metarodingite types underwent variable degrees of retrograde amphibolitization induced by external fluids derived from metasedimentary rocks,

causing Ca depletion and enrichment in Mg, Ba and alkaline elements (Na, K, Cs and Rb).

These geochemical variations reflect the exchange of major and trace elements between different lithologies (serpentinites, metarodingites and metasedimentary rocks) in a subducting slab or slab-mantle interface. Metarodingites may influence the redox state and trace element signature of slab fluids, especially through iron oxidation, fractionation of Sr, Pb and Ba into epidote, and release of Ca and Re in fluids that may induce metasomatism in the sub-arc mantle. Recycling of residual metarodingites in the convective asthenosphere may produce Ca-rich reservoirs in the deep mantle.

Keywords: Cerro del Almirez; rodingite; serpentinite; subduction; fluid; platinum-group elements

1. INTRODUCTION

Rodingites are the product of hydrothermal alteration of igneous mafic to felsic lithologies, usually gabbroic and basaltic rocks, induced by reactive fluids from enclosing peridotites being serpentinized (Coleman, 1967). Rodingites are thus commonly in close association with serpentinites formed at slow mid-ocean ridges (e.g., Frost et al., 2008; Früh-Green et al., 2017), continental passive margins (Beard et al., 2002), or in subduction zones (Koutsovitis et al., 2013; Li et al., 2004, 2007). During rodingitization, the primary mineral assemblage of igneous rocks is mainly replaced by Ca-Al silicates (grossular/hydrogrossular, prehnite, zoisite and vesuvianite), Ca-Mg silicates (diopside and tremolite) and chlorite through metasomatic reactions promoted by highly reducing fluids (e.g., Bach and Klein, 2009; Frost and Beard, 2007). In subduction zones, dehydration of variably altered oceanic lithosphere, which may include serpentinites and metarodingites, releases a significant amount of fluids to the supra-subduction mantle wedge, triggering partial melting and generation of arc magmas (e.g., Hacker et al., 2003; Rüpke et al., 2004; van Keken et al., 2011). Slab fluids commonly transfer the geochemical imprint of subducted lithologies to the sub-arc mantle, causing for instance the enrichment of large-ion lithophile elements (LILE: K, Cs, Rb, Ba and Sr) and Pb in subduction-related lavas compared to mid-ocean ridge basalts (MORB) (e.g., Kelemen et al., 2014), and Mg-Ca-Si metasomatism in the mantle wedge (Ishimaru and Arai, 2011).

The study of the geochemistry of high-pressure metamorphic rocks (metasedimentary, metamafic and metaultramafic rocks, and hybrid lithologies in mélanges) can contribute to constrain the slab component added to arc magma sources, as chemical processing during subduction influences the element budget and isotopic composition of slab fluids and melts (e.g., Bebout, 2014). Petrological and geochemical

studies of element mobility in subducted mafic rocks usually consider starting MORB-like compositions with variable H_2O-CO_2 contents that evolve to blueschist and eclogite mineral assemblages (e.g., Marschall et al., 2006; Schmidt and Poli, 2014; Spandler and Pirard, 2013; Zack et al., 2002). Conversely, the mineralogical and compositional changes undergone by subducting oceanic rodingites, which are notably richer in Ca and poorer in Si, Na, and K than MORB (e.g., Bach and Klein, 2009; Frost and Beard, 2007), are often disregarded in global geochemical balances despite their possible contribution to mass exchanges in subduction zones and to the geochemical signature of arc magmas. Moreover, metasomatic reactions between metarodingite layers and enclosing ultramafic rocks may contribute to the lithological and compositional heterogeneity of subduction mélanges, which may influence the composition of slab fluids (e.g., Bebout and Barton, 2002) and favour the deep transport of volatiles in subduction zones (Spandler et al., 2008).

In this work, we examine the geochemical imprints that seafloor rodingitization, subduction metamorphism and exhumation imposed to the compositions of metarodingites from the Cerro del Almirez ultramafic massif (Betic Cordillera, southern Spain) in terms of major, lithophile and strongly chalcophile trace elements (Re and platinum-group elements, PGE: Os, Ir, Ru, Pt and Pd). This massif preserves an exceptional record of antigorite (Atg) breakdown in subducted serpentinites (Padrón-Navarta et al., 2011; Trommsdorff et al., 1998), which is the most important devolatilization reaction that occurs at intermediate depths in subduction zones (Ulmer and Trommsdorff, 1995). The Almirez metarodingites are enclosed in both Atg-serpentinites and partially dehydrated chlorite (Chl)-harzburgites, and have mineral assemblages that record oceanic rodingitization, prograde metamorphism and interaction with fluids during exhumation (Laborda-López et al., 2018). Therefore, these

rocks represent a unique opportunity to constrain the impact of metarodingites on the geochemical signature of slab material recycled in the mantle and of fluids derived from subducted serpentinites, including the fluid budget of chalcophile metals that may favour the generation of economic ore deposits (McInnes et al., 1999).

2. GEOLOGICAL SETTING

The Nevado-Filábride Complex (NFC) is the lowermost tectono-metamorphic complex of the Internal Zones of the Betic Cordillera (southern Spain). The NFC crops out in the core of several antiformal domes and is separated from the overlying Alpujárride Complex of the allochthonous Alborán Domain by detachment faults (Fig. 1a). The lithological sequence of the NFC mainly consists of metapelites, marbles and orthogneisses derived from the Palaeozoic basement and Mesozoic cover of the southern Iberian paleomargin (e.g., Gómez-Pugnaire et al., 2012; Jabaloy-Sánchez et al., 2018; Santamaría-López and Sanz de Galdeano, 2018). The mineralogy of NFC rocks attests for metamorphism at intermediate- to high-P and different T conditions during the Alpine orogeny, when the SE Iberian paleomargin subducted beneath the extended Alborán Domain and reached peak metamorphic conditions at 18-15 Ma (e.g., Gómez-Pugnaire et al., 2012, 2019; Kirchner et al., 2016; López Sánchez-Vizcaíno et al., 2001; Platt et al., 2006).

The uppermost part of the NFC sequence includes abundant metabasites (eclogites and amphibolites) with remnants of their Jurassic igneous protoliths (Gómez-Pugnaire et al., 2000; Puga et al., 2011), and ultramafic rock bodies (mainly serpentinites) that preserve the imprint of oceanic seafloor alteration prior to the Alpine metamorphism (Alt et al., 2012; Laborda-López et al., 2018; Puga et al., 2011). The Cerro del Almirez massif is the largest (~ 2 km² and 0.4 km thick) of these discontinuous ultramafic outcrops and consists of foliated Atg-serpentinites (~ 200 m

thick) underlain by Chl-harzburgites with either granofels or spinifex-like textures (Fig. 1b, c). The contact between these two lithologies is oblique to the serpentinite foliation and represents the front of antigorite dehydration to olivine + orthopyroxene + chlorite (Fig. 1c) (López Sánchez-Vizcaíno et al., 2005, 2009; Padrón-Navarta et al., 2010a, 2010b, 2011; Trommsdorff et al., 1998). Recently, Bretscher et al. (2018) suggested that this lithological boundary might reflect different original degrees of oxidation during serpentinization at the seafloor. Along the dehydration front, transitional lithologies consisting of chlorite serpentinites and antigorite–chlorite–orthopyroxene–olivine rocks crop out in a zone up to 8 m thick (Padrón-Navarta et al., 2011). Other subordinate lithologies at Cerro del Almirez are centimetric to metric layers of clinopyroxenite and metadunite, and titanian clinohumite–olivine veins. In addition, metarodingite bodies occur as discontinuous layers with maximum 12 m length and 1.8 m thickness hosted in both Atg-serpentinites and Chl-harzburgites (Laborda-López et al., 2018). Stable isotope compositions of serpentinites and thermodynamic modelling of metarodingites support that seafloor serpentinization and rodingitization occurred simultaneously at ~ 150-325 °C, < 2 kbar and reducing conditions (Alt et al., 2012; Laborda-López et al., 2018). Seafloor metamorphism was followed by Alpine subduction to eclogite-facies conditions that caused the Middle Miocene breakdown of antigorite in serpentinites (López Sánchez-Vizcaíno et al., 2001) at ~ 1.7 GPa (~ 60 km depth) and 630-650 °C (Padrón-Navarta et al., 2010a, 2011).

Below we summarize the main mineralogical and petrographic features of the different types of metarodingites from Cerro del Almirez (Fig. 1b, c), as well as those of the spatially associated metasomatic rims and ultramafic rocks. More details on the field occurrences, parageneses, microstructures and major element compositions of minerals in the Almirez metarodingites and ultramafic rocks can be found in Laborda-López et

al. (2018) and Padrón-Navarta et al. (2011), respectively. Details of sampling, analytical techniques, major, trace and chalcophile element data of whole-rocks, and trace element compositions of minerals studied in this work are presented in the Supplementary material.

3. PETROGRAPHY

3.1. Metarodingites

3.1.1. Grandite-metarodingites

Grandite-metarodingite (in the following Grand-metarodingite) consists of grossular and andradite (grandite)-rich garnet + chlorite + diopside + titanite + magnetite + apatite + ilmenite + allanite + zircon + pentlandite + chalcopyrite + pyrrhotite. This is the most abundant type of metarodingites enclosed in Atg-serpentinites and constitutes as well the relic core of some metarodingite boudins in Chl-harzburgites (Fig. 1b, c). Grand-metarodingite has a very fine-grained matrix mostly consisting of allotriomorphic aggregates of anhedral red-brownish garnet (Grt-1) and less abundant diopside locally with tiny exsolutions of magnetite, ilmenite and titanite. Dark pseudomorphs of chlorite + diopside + titanite + magnetite replaced rare phenocrysts of igneous olivine. The most primitive assemblage preserved in Grand-metarodingite (Grt-1 + chlorite + diopside + magnetite + ilmenite) formed during oceanic rodingitization at T = 150-325 °C and P < 2 kbar (Laborda-López et al., 2018). In the most deformed samples, porphyritic igneous textures partially or completely recrystallized to homogeneous granoblastic or slightly oriented microstructures. Two vein generations, corresponding to different garnet compositions (Grt-2 and Grt-3) richer in andradite and pyrope, almandine and spessartine (pyralspite) components than Grt-1, crosscut the matrix and formed during subduction (Laborda-López et al., 2018). The occurrence of accessory epidote marks the transition to Epidote-metarodingites.

3.1.2. Epidote-metarodingites

Epidote-metarodingite (in the following Ep-metarodingite) consists of epidote + diopside + titanite + apatite + zircon + pentlandite + chalcopyrite + pyrrhotite ± garnet ± chlorite ± magnetite ± rutile. Evidence of incipient transformation from Grand- to Ep-metarodingites is visible in almost all Grand-metarodingite outcrops, but this transformation is especially clear in some boudins close to the serpentinite dehydration front. Ep-metarodingite is the most common metarodingite type within Chl-harzburgites (Fig. 1b), where it usually forms the core of boudins that are partially amphibolitized at rims (see section 3.1.4). The matrix is made of epidote and diopside aggregates after garnet, with disseminated chlorite flakes that are less abundant toward the core of the boudins. Small metastable relics of Grt-2 and Grt-3 are present, but garnet in bodies hosted in Chl-harzburgites normally recrystallized to pyralspite-, grossular-rich and andradite-poor compositions (Grt-4). Titanite is more abundant than in Grand-metarodingites.

3.1.3. Pyralspite-metarodingites

Pyralspite-metarodingite (in the following Pyrals-metarodingite) crops out only in the dehydrated Chl-harzburgite domain (Fig. 1b, c). The assemblage of this rock consists of tremolitic amphibole (Amp-1) + epidote + zoisite + new pyralspitic garnet (Grt-5) + rutile + apatite + zircon + pentlandite + chalcopyrite + pyrrhotite + pyrite ± chlorite ± diopside ± magnetite ± titanite. Grt-5 occurs as porphyroblasts with variable grain size and abundant inclusions of Amp-1, chlorite, epidote, zoisite and apatite. The grano- to nematoblastic matrix consists of epidote, Amp-1, and minor chlorite, zoisite, diopside, rutile and apatite.

3.1.4. Mineralogical changes associated with late amphibolitization

Late pargasitic amphibole (Amp-2) is common in all metarodingite types. In Grand-metarodingite, Amp-2 replaces diopside and garnet, in Ep-metarodingite it replaces diopside, and in Pyrals-metarodingite it replaces tremolitic Amp-1 and diopside. The

degree of amphibolitization is, however, very variable and is more intense in Ep- and Pyrals-metarodingites hosted in Chl-harzburgites (Fig. 1b, c).

3.2. Metasomatic reaction rims

Metasomatic reaction rims surround all the metarodingite boudins (Laborda-López et al., 2018, their Fig. 2). From metarodingites to host ultramafic rocks, three metasomatic rock-types are observed: i) chlorite-blackwalls, ii) chlorite-diopside- and iii) chlorite-olivine-diopside-metasomatic rims. All these transitional rinds are located between metarodingites and Atg-serpentinites, and only the first two types occur in the Chl-harzburgite domain.

3.2.1. Chlorite-blackwalls

Chlorite (Chl)-blackwall (5-20 cm thick) is a strongly foliated, chlorite-diopside schist with magnetite + ilmenite ± titanite ± rutile and accessory apatite, zircon, pentlandite, chalcopyrite, pyrrhotite ± pyrite. This rock essentially consists of alternating chlorite- and diopside-rich layers and veins. In some places, rare grains or veins of epidote, amphibole or garnet are visible. Chl-blackwall has lepidoblastic texture marked by the preferred orientation of chlorite flakes. Diopside constitutes hypidiomorphic-xenomorphic isolated grains or granoblastic aggregates. In the Atg-serpentinite domain, oriented titanite (up to 1.5 cm long) and magnetite are abundant, whereas magnetite is scarce in Chl-blackwalls enclosed in Chl-harzburgites. Rutile is especially abundant in blackwalls around Pyrals–metarodingites.

3.2.2. Chlorite-diopside- and chlorite-olivine-diopside-metasomatic rims

Chlorite-diopside- (Chl-Di-) and chlorite-olivine-diopside- (Chl-Ol-Di-) metasomatic rims have variable thickness (2-20 cm). The former is a whitish rock with nematoblastic texture, thin dark layers of chlorite between diopside and disseminated magnetite grains. The first occurrence of millimetre- to centimetre-long brownish aggregates of olivine, in places with titanian-clinohumite lamellae, marks the contact between these lithologies.

Olivine aggregates are embedded in a granoblastic matrix of diopside that has dusty cores and clear rims. Chlorite flakes locally have antigorite relics in the core. The contact with Atg-serpentinite is transitional and defined by increasing antigorite, decreasing diopside and the disappearance of chlorite towards the serpentinite. Within the Chl-harzburgite domain, only a thin band of chlorite-diopside-metasomatic rim is normally visible.

3.3. Host ultramafic rocks

Foliated Atg-serpentinites consist of fine-grained antigorite, minor magnetite, porphyroblastic olivine, and cm-thick veins of olivine locally intergrown with titanian-clinohumite. Diopside and minor tremolite are generally dispersed between antigorite, and diopside can be abundant in serpentinites both close and far from metarodingite bodies.

At the antigorite-out dehydration front, transitional Chl-serpentinite and antigorite–chlorite–orthopyroxene–olivine rock show increasing abundance of chlorite, the sharp growth of prismatic orthopyroxene and steady reduction of antigorite. Late talc replaces orthopyroxene in places, and olivine forms coarse (up to 3 mm) subhedral grains that include antigorite blades (Padrón-Navarta et al., 2011).

Chl-harzburgite mainly consists of brown or clear olivine, orthopyroxene, chlorite, magnetite and accessory ilmenite ± tremolite arranged in a granofelsic or spinifex-like texture (Padrón-Navarta et al., 2011). Some samples include large porphyroblasts of clear olivine and orthopyroxene, which are relics of precursor Atg-serpentinite.

4. RESULTS

4.1. Whole-rock major elements

4.1.1. Metarodingites

There are significant differences between the major element compositions of the metarodingite types from Cerro del Almirez, especially in terms of CaO and SiO_2 (Table S1). Grand-metarodingites have the highest CaO and commonly the lowest SiO_2 contents (Fig. 2a). These compositions are similar to those of rodingites rich in granditic garnet from the seafloor (Früh-Green et al., 2017) and subduction-related terranes (Koutsovitis et al., 2013; Li et al., 2004, 2017), and point to complete seafloor rodingitization at lower temperatures (< 325 ºC, Laborda-López et al., 2018) than those producing epidote-rich rodingites (Bach and Klein, 2009). MgO (Fig. 2b) and Al_2O_3 (Fig. 2c) in Grand-metarodingites have concentrations similar to MORB, basalts from ocean-continent transition zones (OCT) and Mesozoic (non-rodingitized) metamafic rocks from the NFC, but CaO is notably more abundant and SiO_2 (Fig. 2a), Na_2O and K_2O more depleted (Fig. 2c). FeO and Fe_2O_3 contents in Grand-metarodingites vary according to the degree of sample re-equilibration during prograde metamorphism (Laborda-López et al., 2018). The most re-equilibrated samples, with abundant andradite-rich Grt-2 and Grt-3, have high Fe_2O_3 (up to ~ 7 wt.%) and low FeO abundances (~ 2 wt.%) (Fig. 3a). Loss on ignition (LOI) values range from ~ 0.5 wt.% in diopside-rich to 3.7 wt.% in the chlorite-richest sample.

Ep-metarodingites are poorer in CaO and richer in SiO_2 than Grand-metarodingites (Fig. 2a). These concentrations overlap those of epidote-rich rodingites from other localities (Attoh et al., 2006; Fukuyama et al., 2014; Li et al., 2017). Contents of MgO (Fig. 2b), Al_2O_3 (Fig. 2c), FeO and Fe_2O_3 (Fig. 3a) are similar to those of Grand-metarodingites. Loss on ignition values range from ~ 0.3 to 1.6 wt.% and are higher in chlorite-rich samples.

Pyrals-metarodingites are partially amphibolitized. They are generally depleted in CaO (Fig. 2a) and enriched in MgO (Fig. 2b), Na_2O and K_2O (Fig. 2c) compared to

the other metarodingite types, and resemble amphibolitized Ep-metarodingites. In terms of CaO-SiO_2 variations, these rocks overlap the compositions of pyralspite-rich metarodingites from the Cima di Gagnone massif (Fig. 2a) (Evans et al., 1979, 1981). Amphibolitized Pyrals-metarodingites have the highest FeO and lowest Fe_2O_3 contents among the Almirez metarodingites (Fig. 3a).

Amphibolitized samples (mostly derived from Ep-metarodingites) are depleted in CaO (Fig. 2a) and enriched in MgO (Fig. 2b), Na_2O, K_2O (Fig. 2c) and FeO (Fig. 3a) compared to the corresponding non-amphibolitized metarodingite type.

4.1.2. Metasomatic reaction rims and ultramafic rocks

Compared to metarodingites, Chl-blackwalls are enriched in MgO, depleted in CaO (Fig. 2b) and have similar SiO_2 and Al_2O_3 contents (Fig. 3b) (Table S1). Chl-blackwalls hosted in Atg-serpentinites have higher Fe_2O_3 and lower FeO than Chl-blackwalls in Chl-harzburgites (Fig. 3a), in agreement with their higher abundances of magnetite.

Chl-Di-metasomatic rims are richer in CaO (Fig. 2b) and SiO_2 (Fig. 3b) and poorer in Al_2O_3 (Fig. 3b), MnO and TiO_2 than Chl-blackwalls. Chl-Ol-Di-metasomatic rims are poorer in CaO and richer in MgO than Chl-Di-metasomatic rims. Both rock-types have relatively low FeO and high Fe_2O_3 contents, which partially overlap with the values of the host Atg-serpentinites (Fig. 3a).

Atg-serpentinites have similar Al_2O_3 and generally lower SiO_2 and FeO abundances than Chl-serpentinites, Atg-Chl-Opx-Ol rocks and Chl-harzburgites (Fig. 3) (Table S1).

4.2. Whole-rock lithophile trace elements

4.2.1. Metarodingites

The three types of metarodingite present very similar chondrite-normalized rare earth elements (REE) patterns (La_N/Sm_N = 1.14-1.78, Sm_N/Yb_N = 1.37-3.04), akin to those of E-MORB and basalts from OCT, and different from N-MORB (Fig. 4a) (Table S1).

Metarodingites have variable Eu anomalies (Eu_N/Eu^* = 0.87-1.98), which are especially positive in Ep-metarodingites (Eu_N/Eu^* = 1.07-1.64). Amphibolitized samples have REE signatures similar to the corresponding non-amphibolitized metarodingites (Fig. 4a).

Grand-metarodingites are depleted in Cs, Rb and Ba compared to E-MORB, OCT basalts and NFC metamafic rocks, and their normalized patterns present evident negative anomalies of Pb and Sr (Fig. 5a). Ep-metarodingites are richer in Ba than Grand-metarodingites and, opposite to them, show strong positive Pb and Sr spikes (Fig. 5a). Amphibolitized metarodingites have higher concentrations of Cs, Rb and Ba than the corresponding non-amphibolitized samples (Fig. 5a). Amphibolitized Pyrals-metarodingites have lower Sr abundances than amphibolitized Ep-metarodingites (Fig. 5a).

4.2.2. Metasomatic reaction rims

Chl-blackwalls present a large variability in terms of REE concentrations that do not correlate with the type of associated metarodingite or host ultramafic rock (Table S1). Some of their chondrite-normalized REE patterns resemble those of metarodingites but have more variable LREE/MREE and MREE/HREE fractionations (La_N/Sm_N = 0.47-2.56, Sm_N/Yb_N = 1.13-3.52) (Fig. 4b). The rest of Chl-blackwalls have notably lower REE abundances and are relatively depleted in LREE (La_N/Sm_N = 0.37-0.63, except one sample with La_N/Sm_N = 1.25) and HREE (Sm_N/Yb_N = 1.40-4.05) (Fig. 4b). The Eu anomaly of these patterns is variable (Eu_N/Eu^* = 0.40-1.50) but is usually negative in the REE-depleted samples (Fig. 4b).

Chl-Di- and Ch-Ol-Di-metasomatic rims have normalized REE patterns similar to Chl-blackwalls depleted in REE (La_N/Sm_N = 0.31-0.64), but in general have lower REE concentrations and are less MREE/HREE fractionated (Sm_N/Yb_N = 1.04-1.26)

(Fig. 4b). Their compositions are transitional to those of Atg-serpentinites, and, similar to the latter, they present negative Eu anomalies (Fig. 4b).

Chl-blackwalls and Chl-(± Ol-)Di-metasomatic rims have Cs, Rb and Ba concentrations similar to metarodingites (Fig. 5b), but Chl-(± Ol-)Di-metasomatic rims normally have lower Cs and Rb concentrations than Chl-blackwalls (Fig. 5b). Thorium and U have higher concentrations in REE-rich than in REE-poor Chl-blackwalls. On the other hand, high field strength elements (HFSE: Nb, Ta, Zr and Hf) are systematically more abundant in Chl-blackwalls than in Chl-Di- and Chl-Ol-Di-metasomatic rims, irrespective of their REE contents, and have concentrations similar to metarodingites (Fig. 5b). Lead in the normalized patterns of Chl-blackwalls shows positive or negative spike relative to LREE, whereas it is systematically enriched in Chl-Di- and Chl-Ol-Di-metasomatic rims (Fig. 5b). On the contrary, Sr is relatively depleted in both Chl-blackwalls and Chl-(± Ol-)Di-metasomatic rims (Fig. 5b).

4.2.3. Host ultramafic rocks

Atg-serpentinites are normally depleted in LREE relative to MREE (La_N/Sm_N = 0.30-1.27) and in MREE relative to HREE (Sm_N/Yb_N = 0.63-1.18) (Fig. 4c) (Table S1). All patterns of Atg-serpentinites show negative Eu anomalies (Fig. 4c). Chl-serpentinites, Atg-Chl-Opx-Ol rocks and Chl-harzburgites are normally depleted in LREE and MREE and more MREE/HREE fractionated (Sm_N/Yb_N = 0.10-0.66) compared to Atg-serpentinites (Fig. 4c, d) (see also Garrido et al., 2005 and Marchesi et al., 2013), except two Chl-harzburgites with abundant tremolite (Fig. 4d). Chl-harzburgites are generally richer in LREE and MREE than transitional Chl-serpentinite and Atg-Chl-Opx-Ol rocks (compare Fig. 4c and d). Similar to Atg-serpentinites, these rocks present negative Eu anomalies (Fig. 4c, d).

Atg-serpentinites usually have lower Cs, Rb, Th, U, Nb and Ta concentrations than transitional Chl serpentinite and Atg-Chl-Opx-Ol rocks (Fig. 5c). Lead shows positive anomaly in the patterns of these lithotypes, whereas Sr is enriched relative to LREE in transitional rocks and depleted in Atg-serpentinites (Fig. 5c). As noted by Garrido et al. (2005) and Marchesi et al. (2013), Chl-harzburgites are enriched in Th, U, Nb and Ta compared to Atg-serpentinites (Fig. 5d). Similar to serpentinites, Chl-harzburgites have patterns with positive spike of Pb, while Sr is more variable (Fig. 5d).

4.3. Lithophile trace elements in minerals

4.3.1. Garnet

Garnets of Grand-metarodingites (Grt-1, Grt-2 and Grt-3) are all enriched in MREE and HREE relative to LREE (La_N/Sm_N = 0.005-0.014, La_N/Yb_N = 0.24-0.92) (Table S2), but their REE patterns have some differences (Fig. 6a). Grt-1 has higher HREE and lower MREE concentrations than Grt-2, and both have negative Eu anomaly (Eu_N/Eu^* = 0.48–1.02). Grt-3 has concentrations of LREE similar to Grt-1 and Grt-2, but is notably more depleted in MREE and HREE and has slightly positive Eu anomaly (Eu_N/Eu^* = 1.15–1.56). All these garnet types are enriched in Th, U, Nb, Ta, Zr and Hf compared to adjacent elements in the normalized patterns (Fig. 6b). Strontium in Grt-1 and, especially, Grt-2 displays a pronounced negative anomaly. Grt-3 has lower Ba, Th, Nb and Ta abundances than Grt-1 and Grt-2, and evident negative anomalies of Pb and Sr (Fig. 6b). Progressive depletion in Sr and Ba from Grt-1 to Grt-3 (Fig. 6b) correlates with slightly decreasing Ca abundances in successive garnet generations (Laborda-López et al., 2018).

Grt-2 in Ep-metarodingites is notably more depleted in LREE, MREE (Sm_N/Yb_N = 0.001-0.03) (Fig. 6a), Th, U, Nb, Ta and Hf than Grt-2 in Grand-metarodingites, and is also normally enriched in Pb and Sr compared to the latter (Fig. 6b). More pyralspitic Grt-4 and Grt-5 in Ep- and Pyrals-metarodingites, respectively, have LREE-MREE

compositions similar to Grt-2 in Ep-metarodingites but higher HREE abundances (Fig. 6a). These types of garnet also have Cs, Rb, Ba, Th, U, Nb and Ta concentrations similar to Grt-2 in Ep-metarodingites but lower Pb, Sr, Zr and Hf abundances (Fig. 6b).

4.3.2. Allanite and epidote

Allanite in Grand-metarodingites is extremely rich in LREE and MREE (La_N/Sm_N = 8.01–19.32, Sm_N/Yb_N ~ 1000-10000) (Table S2) and presents negative Eu anomaly (Eu_N/Eu^* = 0.49–0.77) (Fig. 7a). Normalized patterns of this mineral show prominent positive spikes of Th and U and negative peaks of Nb, Ta, Pb, Sr, Zr and Hf (Fig. 7b).

Epidote has similar trace element compositions in Ep- and Pyrals-metarodingites (Table S2). This phase is generally enriched in LREE and MREE compared to HREE (La_N/Yb_N = 1.33–66.55, Sm_N/Yb_N = 1.15-47.9), except rare epidote in veins (La_N/Yb_N = 0.47–1.58, Sm_N/Yb_N = 0.42-0.92), and commonly shows positive Eu anomaly (Eu_N/Eu^* = 0.92-2.56) (Fig. 7a). Epidote is poor in Th, U, LREE and MREE, and rich in Ba, Pb, Sr and HREE compared to allanite (Fig. 7).

4.3.3. Diopside and amphibole

Diopside in Grand-metarodingites has lower REE concentrations than chondrite (Fig. 8a) (Table S2). This phase is enriched in MREE compared to LREE and HREE (La_N/Sm_N = 0.06-0.16, Sm_N/Yb_N = 23.4-50.0) (Fig. 8a), and in Pb and Sr relative to adjacent elements in the normalized patterns (Fig. 8b). Late amphibole (Amp-2) in Grand-metarodingites is enriched in REE (especially HREE) (Fig. 8a), Rb, Ba, U and Sr compared to diopside in the same rocks (Fig. 8b) (Table S2).

Diopside in Ep-metarodingites is depleted in LREE and MREE and enriched in HREE relative to diopside in Grand-metarodingites, and displays variable MREE/HREE fractionation (Sm_N/Yb_N = 0.27-2.12) (Fig. 8a) and normally positive Eu anomaly (Eu_N/Eu^* = 0.96-2.28). Similar to diopside in Grand-metarodingites, this phase is relatively rich in Pb and Sr (Fig. 8b).

Diopside in Pyrals-metarodingites is enriched in MREE and HREE and has similar LREE concentrations compared to diopside in Grand-metarodingites, and presents evident Eu negative anomaly (Eu_N/Eu^* = 0.45-0.60). MREE/HREE fractionation is variable (Sm_N/Yb_N = 0.84-2.57) (Fig. 8a). Rubidium, Ba, U, Pb and Sr are enriched relatively to adjacent elements (Fig. 8b). Amp-2 in Pyrals-metarodingites has lower LREE and MREE concentrations than diopside in the same rocks and presents variable Eu anomaly (Eu_N/Eu^* = 0.67-1.19) (Fig. 8a). Rubidium, Ba, Nb, Ta, Zr and Hf are enriched in Amp-2 compared to concentrations in diopside (Fig. 8b).

4.4. PGE-Re abundances and Os isotopes in whole-rocks

All metarodingite types from Cerro del Almirez have similar PGE-Re concentrations (between 10^{-4} and 10^{0} the primitive upper mantle (PUM) values) (Table S3) that are analogous to those of MORB, except for lower contents of Re (Fig. 9a). Their normalized PGE-Re patterns are depleted in Os, Ir and Ru (I-PGE) compared to Pt, Pd (P-PGE) and Re (e.g., Pt_N/Os_N = 1.1-9.8), except in one atypical Os-rich Grand-metarodingite (AL14-16 with Pt_N/Os_N = 0.2). Ep-metarodingites have slightly lower Pt concentrations than the other metarodingite-types (Fig. 9a).

Independently from their REE contents, Chl-blackwalls have PGE-Re abundances very similar to metarodingites (Fig. 9b) (Table S3). These rocks are depleted in Ir compared to Os and have P-PGE concentrations similar to or lower than Ep-metarodingites (Fig. 9b). Chl-(± Ol-)Di-metasomatic rims have PGE concentrations two to four orders of magnitude higher than metarodingites and Chl-blackwalls, and very similar to those of depleted MORB mantle (DMM) (Fig. 9b). Their normalized patterns are commonly flat (Pt_N/Os_N = 1.0-1.1) except for one sample with lower I-PGE contents (AL14-23 with Pt_N/Os_N = 4.4) (Fig. 9b). Rhenium in Chl-(± Ol-)Di-metasomatic rims is significantly depleted relative to Pd.

Atg-serpentinites have PGE-Re concentrations very similar to those of DMM and Chl-(± Ol-)Di-metasomatic rims (Fig. 9c). Chl-harzburgites have PGE-Re compositions also similar to DMM but they are more heterogeneous compared to Atg-serpentinites, especially in terms of Pd (Fig. 9d) (Table S3).

The present-day $^{187}Os/^{188}Os$ ratios of metarodingites, which are controlled by the time-integrated decay of ^{187}Re to ^{187}Os, are very variable (0.1993-1.0721) and notably higher than the chondritic (0.1270, Shirey and Walker, 1998) and DMM values (0.1281, Walker et al., 2002) (Fig. 10) (Table S3). These Os isotopic compositions are unrelated to the metarodingite type and coincide with those of Chl-blackwalls (Fig. 10). Higher Os concentrations in Chl-(± Ol-)Di-metasomatic rims are coupled to significantly lower $^{187}Os/^{188}Os$ (0.1248-0.1341) (Fig. 10) (Table S3). Atg-serpentinites and Chl-harzburgites have subchondritic Os isotopic compositions ($^{187}Os/^{188}Os$ = 0.1189-0.1258) lower than DMM and similar to Chl-(± Ol-)Di-metasomatic rims (Fig. 10) (Table S3).

5. DISCUSSION

Metarodingites, metasomatic rims and host ultramafic rocks from Cerro del Almirez underwent a complex petrological evolution from seafloor hydrothermal alteration to subduction metamorphism in the eclogite facies, and exhumation (Laborda-López et al., 2018; Padrón-Navarta et al., 2011). During this evolution, metasomatic and metamorphic reactions involving fluids with different oxidizing capacities occurred in the metarodingite-ultramafic suites. The geochemical data presented in this work permit to infer how the main stages of this evolution, including the exceptionally well documented dehydration of Atg-serpentinites, affected the bulk and mineral compositions of these rocks (Figs. 11 and 12). The discussion of these results aims to constrain for the first time the role of subducted metarodingites in the geochemical

signature of slab fluids, including their redox state, and element recycling at different depths in subduction zones.

5.1. Seafloor rodingitization

5.1.1. Lithophile elements

The igneous protoliths of the Almirez metarodingites were mafic rocks with different proportions of plagioclase, clinopyroxene and olivine arranged in doleritic or porphyritic textures (Laborda-López et al., 2018). Rodingitization of these mafic intrusions was concomitant with seafloor serpentinization of enclosing ultramafic rocks (Alt et al., 2012) due to mantle exhumation by continental rifting (Gómez-Pugnaire et al., 2000) or ultra-slow oceanic spreading (Puga et al., 2011). This extensional event produced mafic intrusions of Jurassic age (~ 185 Ma) with E- or T-MORB geochemical signature (Puga et al., 2011) likely emplaced in an ocean-continent transition zone (OCT, Fig. 11a) or at a tectonically similar (Manatschal and Müntener, 2009) ultra-slow spreading centre. To assess the chemical variations induced by seafloor rodingitization, we compare the compositions of Grand-metarodingites with those of representative MORB, OCT basalts and Mesozoic (non-rodingitized) metamafic rocks from the NFC. This comparison supports that, among major elements, seafloor rodingitization by reducing fluids (Frost and Beard, 2007) caused prominent Si, Na and K loss and Ca enrichment in metarodingites (Fig. 2a, c) by element transfer during coeval serpentinization of host peridotites (Fig. 11b, c) (Bach and Klein, 2009; Evans et al., 1981; Tang et al., 2018).

Whole-rock REE concentrations in Grand-metarodingites match those of E-MORB, OCT basalts and NFC metamafic rocks (Fig. 4a), supporting that REE remained immobile during rodingitization of the core portion of the mafic intrusions (e.g., Evans et al., 1981; Fukuyama et al., 2014; Koutsovitis et al., 2018; Pusching, 2002). Moreover, LREE and HREE in Grand-metarodingites correlate with elements

similarly incompatible during mantle melting, such as Nb and V respectively (Fig. S1). The latter elements are commonly not mobilized in aqueous fluids at low pressure (Niu, 2004), supporting that REE patterns in the core of Grand-metarodingite bodies mostly preserve the signature of their igneous protoliths.

Similar to Na and K (Fig. 2c), Cs, Rb, Ba and Sr are notably depleted in Grand-metarodingites compared to MORB, OCT basalts and NFC metamafic rocks (Fig. 5a), supporting that LILE were remobilized during rodingitization (Fig. 11c) (e.g., Austrheim and Prestvik, 2008; Evans et al., 1981; Puschnig, 2002) and incorporated into enclosing serpentinites (Marchesi et al., 2013). We ascribe this behaviour to the breakdowns of main igneous minerals, namely plagioclase and clinopyroxene, to an assemblage dominated by granditic Grt-1, chlorite and diopside during complete rodingitization (Laborda-López et al., 2018). Through these reactions, alkaline metals, LILE and Pb were mobilized into the fluid phase (Fig. 11c) as they are incompatible in Grt-1 (Fig. 6b) and only in part incorporated into less abundant diopside (especially Sr and Pb) (Fig. 8b). Depletion of these elements might have occurred in part during successive subduction metamorphism but the absence of mineral phases capable to retain LILE during rodingitization supports that their main loss occurred at this stage.

5.1.2. PGE-Re abundances and Os isotopes

Concerning strongly chalcophile elements, hydrothermal alteration at reducing conditions, like those that characterize oceanic rodingitization, is not expected to change the PGE abundances of igneous mafic rocks (Peucker-Ehrenbrinck et al., 2003), but may cause important uptake of Re from seawater (Reisberg et al., 2008). Metarodingites from Cerro del Almirez have PGE patterns that overlap the compositions of MORB (Fig. 9a), pointing to immobility of PGE during rodingitization (and subduction). However, opposite to the trend caused by reducing hydrothermal alteration, Re is

generally more depleted in these rocks than in MORB (Fig. 9a) suggesting that Re was lost after igneous crystallization. Using the measured Re/Os ratio of metarodingites to calculate $^{187}Os/^{188}Os$ back to the age of intrusion (185 Ma, Puga et al., 2011) results in $^{187}Os/^{188}Os_{(185\ Ma)}$ = 0.1969-0.8864, which are notably higher than values expected for magmas derived from DMM-like sources (~ 0.130) (Gannoun et al., 2016). These high initial $^{187}Os/^{188}Os$ can be either due to incorporation of radiogenic Os from Jurassic seawater, or lowering of the Re/Os ratios long after the magmatic emplacement, likely during Alpine subduction. Osmium uptake from seawater occurs by precipitation of Fe-Mn oxyhydroxides at oxidative conditions (Ravizza et al., 2001), which are very different from the low fO_2-conditions of oceanic rodingitization (Frost and Beard, 2007). We thus conclude that seafloor rodingitization did not significantly influence the primary igneous budget of Re and PGE, but metarodingites likely experienced Re loss during subduction by mobilization in oxidizing fluids (see section 5.3.) (Reisberg et al., 2008).

5.2. Element mobility at the rodingite-serpentinite interface

Metasomatic reaction rims are present at the contact between metarodingites and enclosing ultramafic rocks (Fig. 11c). Metasomatic exchanges between mafic and chemically distinct rocks at the seafloor and during subduction can be driven by strong gradients of chemical potentials of major elements and are favoured by infiltration of aqueous fluids (e.g., Bebout and Barton, 2002; Penniston-Dorland et al., 2014; Spandler et al., 2008). Replacement of primary minerals by Ca-Al-rich phases during rodingitization further promotes metasomatic alteration at the contact between serpentinite and rodingitized igneous intrusions (Boschi et al., 2006).

Along with usually fluid-immobile HFSE, strongly chalcophile elements can reveal the nature of the protoliths of metasomatic rims as they commonly preserve the

imprint of their source material (Penniston-Dorland et al., 2012, 2014). Irrespective of their variable REE contents (Fig. 4b), Chl-blackwalls from Cerro del Almirez have abundances of HFSE (Fig. 5b), PGE-Re (Fig. 9b), and Os isotopes (Fig. 10) that match those of metarodingites. This coincidence indicates that Chl-blackwalls formed by massive precipitation of chlorite in the external portion of the mafic bodies, mainly triggered by chemical potential gradient of Mg toward the rodingite at the seafloor and during subduction (Fig. 11c, d). The variable modal abundances of chlorite and diopside in Chl-blackwalls at the sample scale (5-20 cm) (Laborda-López et al., 2018) point to heterogeneous degrees of chloritization in different portions of the mafic layers. Stronger chemical potential gradients and higher integrated fluid/rock ratios at the original rodingite-serpentinite interface likely led to greater precipitation of hydrous chlorite than inward the rodingite bodies (Fig. 11c). Rare earth elements (plus Th and U, Fig. 5b) of rodingite rims in contact with serpentinite were thus remobilized in fluids, possibly as chloride complexes (Haas et al., 1995), as they could not be incorporated into the new mineral assemblage dominated by chlorite. On the other hand, Chl-blackwalls richer in diopside from the inner portions of low permeable rodingites mostly retained the original trace element abundances of their protoliths (Fig. 5b). Higher fluid/rock ratios (and consequently higher Cl^- concentrations) during initial formation of REE-poor Chl-blackwalls at the seafloor are also supported by their negative Eu anomaly opposed to general positive Eu anomaly in REE-rich Chl-blackwalls (Fig. 4b). These negative anomalies suggest Eu incorporation into hydrothermal fluids in the soluble Eu^{2+} state that forms strong aqueous complexes with dissolved Cl at reducing conditions (Allen and Seyfried, 2005), in agreement with the low fO_2 conditions of rodingitization of Grand-metarodingites (Laborda-López et al., 2018).

Normalized patterns of strongly chalcophile elements and Os isotopes of Chl (± Ol)-Di-metasomatic rims are very similar to those of Atg-serpentinites (Figs. 9b, c and 10). These rocks thus most likely formed by massive precipitation of diopside and chlorite in previous serpentinites triggered by strong gradients of Ca and Al chemical potentials toward the ultramafic rock at the seafloor and during subduction (Fig. 11c, d). Diopside in these rocks likely captured most of the trace elements (especially REE) liberated by rodingites transformed to Chl-blackwalls, thus increasing their bulk concentrations compared to precursor serpentinites (Fig. 5c).

During subduction, metasomatic reaction rims and metarodingites likely experienced local mechanical mixing assisted by fluids (Laborda-López et al., 2018, their Fig. 2c). This interaction is suggested by the especially higher Os concentrations and lower $^{187}Os/^{188}Os$ in one Grand-metarodingite sample (AL14-16) (Figs. 9a and 10), and the lower Os-Ir-Ru abundances and higher Os isotopic ratios in one Chl-Ol-Di-metasomatic rim (AL14-23) (Figs. 9b and 10) compared to other samples of the same lithologies. The Os signature of AL14-16 is reproduced by simple mixing of typical metarodingite with ~ 3% Os from Chl-Di-metasomatic rim, and the I-PGE composition of AL14-23 supports contamination of a typical Chl-Ol-Di-metasomatic rim with ~ 80% of Chl-blackwall component. Deformation and shearing during subduction (Fig. 11d) likely produced physical mixing between these lithologies, which was favoured by the abundance of weak layers rich in chlorite that caused juxtaposition of close lithologies at the sample scale (Bebout and Barton, 2002; Penniston-Dorland et al., 2012). Mechanical mixing likely occurred in the presence of fluids able to enrich the rock in mobile elements (Gorman et al., 2019), as was possibly the case of Pt and Pd that have higher concentrations in AL14-23 than in the other metasomatic rims (Fig. 9b).

5.3. Geochemical evolution of Grand-metarodingites during subduction

After seafloor rodingitization, Grand-metarodingites underwent subduction metamorphism at increasing P-T up to ~1.6-1.9 GPa and 620-630 ºC (Laborda-López et al., 2018). The most significant compositional changes that occurred in Grand-metarodingites during subduction were the increase of Fe_2O_3 and decrease of FeO contents due to interaction with oxidizing fluids released by the prograde transformation of lizardite to antigorite and subsequent brucite breakdown in host serpentinites (Fig. 11d) (Laborda-López et al., 2018). Higher andradite and lower grossular components in Grt-2 and Grt-3 than in Grt-1 reflect the relative high fO_2 composition of fluids that precipitated these new garnet-types in veins (Laborda-López et al., 2018).

As noted in section 5.1.2, the Almirez metarodingites are relatively depleted in Re compared to MORB (Fig. 9a). These low Re abundances are not due to subaerial volcanic degassing (Sun et al., 2003) as the igneous protoliths of the Almirez metarodingites were doleritic dykes intruded into peridotites below the seafloor (Fig. 11b) (Puga et al., 2011). Therefore, rhenium in metarodingites was most likely lost during subduction (Fig. 11d). Subducted metabasalts equilibrated at blueschist or eclogite facies conditions lost 40-90% of their original Re budget (Becker, 2000; Dale et al., 2007), especially in samples derived from basalts strongly affected by hydrothermal alteration (Dale et al., 2009). Subducted metarodingites from Cerro del Almirez, whose protoliths were pervasively altered close to the seafloor, thus likely experienced similar depletion in Re. As consequence of Re loss during Miocene subduction, i.e. long after the igneous crystallization of their protoliths in the Early Jurassic (Puga et al., 2011), the Almirez metarodingites have Re/Os ratios that are too low to explain their radiogenic Os isotope compositions (Fig. 10). In particular, metarodingites lost on average ~ 80% of Re necessary to obtain initial $^{187}Os/^{188}Os_{(185\ Ma)}$ around the values expected for Jurassic MORB (~ 0.130) (Gannoun et al., 2016). Partial

replacement of Grt-1 induced by flux of external oxidizing fluids may have caused this important loss of Re (Fig. 11d), as Re is mobile at oxidizing conditions (Reisberg et al., 2008) and Al-garnet is a primary repository of Re in subducted mafic rocks (Dale et al., 2009; Righter and Hauri, 1998). Flux of Re from subducting metarodingites to the mantle wedge may contribute to Re metasomatism in arc peridotites and to generation of Re-rich magmas (Sun et al., 2003).

5.4. Metarodingite evolution during dehydration of enclosing antigorite serpentinites

The circulation of fluids released during dehydration of Atg-serpentinites and their transformation to Chl-harzburgites produced significant changes in the whole-rock and mineral compositions of enclosed metarodingites. These changes were driven by the increase of SiO_2 and decrease of CaO chemical potentials at H_2O-saturated and high fO_2 conditions favoured by the flux of abundant fluids from dehydrating serpentinites (Laborda-López et al., 2018). The interaction of metarodingites with these oxidizing fluids produced the replacement of granditic garnets (Grt-1, Grt-2 and Grt-3) by epidote/clinozoisite and of chlorite by diopside, leading to the oxidation of ferrous iron. These processes finally resulted in the formation of Ep-metarodingites from precursor Grand-metarodingites at ~ 1.6-1.9 GPa and 630-650 °C (Laborda-López et al., 2018). The extent of this transformation is related to the abundance of fluids in the system, and is thus only incipient in many metarodingite bodies enclosed in Atg-serpentinites and well developed in boudins close to the serpentinite dehydration front (Fig. 1c).

In terms of major elements, the transition of Grand- to Ep-metarodingites mainly caused Ca-Mn depletion, related to the replacement of granditic garnets, and enrichment in Si (Fig. 2a) leading to crystallization of new diopside. Except for Eu concentrations, no appreciable differences exist between Grand- and Ep-metarodingites in terms of whole-rock REE abundances (Fig. 4a), supporting that REE in metarodingites were

mostly not mobilized by interaction with serpentinite-derived fluids. However, Ep-metarodingites are notably enriched in Sr, Pb and Ba compared to Grand-metarodingites (Fig. 5a), supporting that they partitioned these elements from serpentinite-derived fluids (Fig. 12a). The mobility of Si, Sr, Pb and Ba in serpentinite-derived fluids is confirmed by their abundance in fluid inclusions from high-pressure Chl-harzburgites generated by antigorite breakdown (Scambelluri et al., 2001, 2015). These inclusions also bear Cl-apatite (Scambelluri et al., 2001), supporting that Ca was mobile in the dehydrating system and fluids were rich in Cl that promoted the mobility of trace elements (Kendrick al., 2011).

Ep-metarodingites also have mostly lower Pt concentrations than Grand-metarodingites (Fig. 9a) suggesting that fluids mobilized Pt (Fig. 12a). Platinum loss in metabasalts equilibrated at eclogite facies conditions has been ascribed to flux of a sulphur-rich oxidizing fluid (Dale et al., 2009). Relatively oxidizing fluids produced by Atg-breakdown have a significant budget of sulphur (Alt et al., 2012, 2013; Schwarzenbach et al., 2018) and may be able to slightly remobilize Pt as bisulfide complexes (Pan and Wood, 1994), especially in deformed metamafic rocks derived from highly altered protoliths (Dale et al., 2009) such as metarodingites from Cerro del Almirez. Serpentinite-derived fluids may then possibly transfer Pt from subducting mafic rocks, including metarodingites, to other lithologies in the slab or over greater distance in the subduction zone.

5.5. Formation of Pyralspite-metarodingites and open-system late amphibolitization

Rare bodies of Pyrals-metarodingites occur exclusively within the Chl-harzburgite domain. The gradients of chemical potentials of major elements (mainly Mg and Ca) between metarodingites and host Chl-harzburgites controlled the formation of Pyrals-metarodingites from Ep-metarodingites at peak metamorphic conditions (~ 1.6-1.9 GPa,

660-685 °C) (Laborda-López et al., 2018). These gradients induced the loss of Ca (Fig. 2a), the incorporation of Mg (Fig. 2b) and the reduction of Fe^{3+} in metarodingites (Fig. 3a) at fluid saturation conditions. The other differences in terms of major elements between Ep- and Pyrals-metarodingites are due to late amphibolitization (see below).

Whole-rock concentrations of REE in Pyrals-metarodingites are similar to those of the other metarodingite-types (Fig. 4a), pointing to no remobilization of REE at peak metamorphic conditions. Contrary to REE, whole-rock Sr concentrations are lower in Pyrals-metarodingite than in Ep-metarodingite (Fig. 5a), due to lower amounts of epidote partially replaced by Grt-5 that is poor in Sr (Fig. 6b). Therefore, the formation of Pyrals-metarodingites from precursor Ep-metarodingites induced the release in fluids of elements mainly hosted in epidote, such as Ca, Sr and most probably Pb, and the incorporation of Mg likely from enclosing Chl-blackwalls (Fig. 12b).

After the formation of the main mineral assemblages, pargasitic amphibole (Amp-2) crystallized in all metarodingite types at retrograde conditions (Laborda-López et al., 2018). These variably amphibolitized samples have compositional differences compared to non-amphibolitized corresponding metarodingites. In terms of major elements, amphibolitization mainly caused enrichment in Mg (Fig. 2b), Na, K (Fig. 2c), Fe^{2+} (Fig. 3a), and depletion of Ca (Figs. 2a and 12c). On the other hand, REE remained immobile (Fig. 4a). Amphibolitization also caused whole-rock enrichment in Cs, Rb and Ba (Figs. 5a, 12c) that are notably partitioned in Amp-2 (Fig. 8b). These compositional changes are due to fluxing of external fluids from metasedimentary rocks (metapelites and metaevaporites) into the ultramafic-metarodingite system (Laborda-López et al., 2018), which led to retrograde crystallization of Amp-2 possibly from P-T conditions close to antigorite breakdown in serpentinites (Marchesi et al., 2013). This scenario is similar to that envisioned for the Cima di Gagnone Chl-harzburgites, which

have relatively radiogenic Sr and Pb isotopic signatures due to prograde interaction with fluids from host metapelites (Cannaò et al., 2015). Interaction of metarodingites from Cerro del Almirez with fluids from metasedimentary rocks continued during exhumation, when the Almirez ultramafic section was tectonically joined to subducted micaschists (Jabaloy-Sánchez et al., 2015).

5.6. Intermineral distribution of trace elements in metarodingites

Fluid-rock interaction during seafloor rodingitization and subduction metamorphism not only caused the loss or gain of major and trace elements in whole-rocks, but also their redistribution between minerals at the sample scale. Taking into account the uncertainties on modal proportions (Laborda-López et al., 2018) and the variabilities of trace element compositions of minerals (Figs. 6, 7 and 8), mass balance calculations show that Grt-1, which formed during rodingitization, concentrates ~ 70 wt.% of whole-rock HREE in Grand-metarodingites (Table S4). These high concentrations of HREE are typical of Al-rich hydrothermal garnets similar to Grt-1 (with up to 70-73 mol.% grossular component, Laborda-López et al., 2018), and indicate prolonged fluid-rock interaction in a system buffered by the rock composition (Gaspar et al., 2008). Relative high contents of HFSE in Grt-1 (Fig. 6b) characterize granditic garnets with high amounts of Ti-rich components (Marks et al., 2008) (up to 11 mol.% in Grt-1, Laborda-López et al., 2018), but the budget of these elements in Grand-metarodingites is most likely controlled by accessory titanite and zircon. Relatively high andradite and lower grossular components in Grt-2 and Grt-3, which crystallized during subduction mostly in veins, explain their high MREE/HREE ratios (Fig. 6a), as thermodynamic data support that HREE are less compatible in Fe^{3+}-rich garnet generated at relatively high fluid/rock ratios (Gaspar et al., 2008). Despite this restriction, mass balance shows that Grt-2 and Grt-3 still host ~ 25 wt.% and 5 wt.% of HREE in Grand-metarodingites,

respectively (Table S4). Middle rare earth elements captured in veins of Grt-2 (~ 30-40 wt.% of whole-rock budget) and Grt-3 (~ 10-25 wt.%) during subduction were likely remobilized in fluids due to the ongoing breakdown reaction of diopside (Laborda-López et al., 2018). Diopside in Grand-metarodingites is actually depleted in all REE, especially HREE (Fig. 8a), due to concomitant crystallization and subsequent metamorphic re-equilibration with Grt-1, Grt-2, Grt-3 and allanite (see below). In this aspect, diopside in Grand-metarodingite is similar to clinopyroxene in common subducted metamafic rocks, in which the contribution of clinopyroxene to the whole-rock budget of REE is minor or negligible (e.g., Hermann, 2002; Spandler et al., 2003; Tribuzio et al., 1996). Grand-metarodingites also include accessory allanite apparently in textural equilibrium with Grt-1. Allanite in subducted mafic rocks is normally stable from blueschist to eclogite facies conditions up to ~ 4.5 GPa and 1000 ºC (Hermann, 2002; Spandler et al., 2003; Tribuzio et al., 1996), suggesting that this phase might have crystallized during subduction. Mass balance calculations show that allanite, despite its very low modal amount (~ 0.1%), hosts ~ 85-100 wt.% of bulk LREE and Th in Grand-metarodingites (Table S4). The presence of this accessory phase thus supports that metarodingites did not liberate significant amounts of LREE and Th into fluids during subduction up to ~ 1.7 GPa. This behaviour is similar to that envisaged for eclogites and metapelites (Hermann, 2002; Spandler et al., 2003; Tribuzio et al., 1996) and is consistent with the relatively high LILE/LREE and low Th/U ratios in arc lavas generated from mantle sources contaminated by slab fluids (e.g., Elliott et al., 1997; Pearce and Peate, 1995).

Intense flux of fluids liberated by antigorite-breakdown in host serpentinites triggered the formation of Ep-metarodingites and promoted the redistribution of REE in their new mineral assemblage, especially into epidote (Fig. 7a), garnet (Fig. 6a) and

likely titanite (Spandler et al., 2003). Mass balance shows that epidote hosts almost all LREE, ~ 80-100 wt.% of MREE and 45-70 wt.% of HREE, and garnet and titanite accommodate the rest of the REE budget of Ep-metarodingites (Table S4). Epidote in these metarodingites is slightly enriched in Eu (Fig. 7a) similar to epidote in hydrothermal veins (Frei et al., 2004). This Eu enrichment, evident also in some whole-rock Ep-metarodingites (Fig. 4a) and in diopside (Fig. 8a), possibly reflects early crystallization of titanite that generates a positive Eu anomaly in the residual fluid and in minerals crystallizing with or after titanite (Loader et al., 2017). Almost all Sr, Pb, and ~ 90 wt.% of Ba in Ep-metarodingites are hosted in epidote, which likely incorporated these elements from fluids by simple homovalent substitution for Ca^{2+} (Frei et al., 2004).

Finally, in Pyrals-metarodingites, which derive from Ep-metarodingites by partial epidote breakdown to new pyrrhotitic garnet (Grt-5) and diopside transformation to tremolitic amphibole (Amp-1) (Laborda-López et al., 2018), REE were partitioned mainly between epidote (~ 95-100 wt.% of LREE and MREE, and 65-90 wt.% of HREE), Grt-5 (~ 5-30 wt.% of HREE) and Amp-1/diopside (~ 1-5 wt.% of MREE and HREE) (Table S4).

5.7. The role of metarodingites in the fluid-mediated element recycling in subduction zones

During subduction, mantle and crustal rocks in the slab and slab-mantle interface experience successive metamorphic reactions that release fluids to the supra-subduction mantle wedge and promote recycling of mobile elements (e.g., B, Li, As, Sb and LILE) in the sources of arc magmas (Fig. 12d) (e.g., Scambelluri and Tonarini, 2012; Schmidt and Poli, 2014; Spandler and Pirard, 2013). Subducted serpentinites and subduction mélanges with serpentinite matrix commonly contain metarodingites (e.g., Cannaò et al., 2015; Hu et al., 2017; Koutsovitis et al., 2013; Li et al., 2007; Scambelluri and

Rampone, 1999; Zanoni et al., 2016), but the role of these rocks in the geochemical processes occurring in subduction zones has generally been neglected. This scarce attention is possibly due to the lower abundance of rodingites in the oceanic crust compared to mafic rocks less affected or undisturbed by hydrothermal alteration. For instance, metarodingites constitute only ~ 0.03% of the outcropping surface in the Cerro del Almirez ultramafic massif. However, field observations show that metarodingites may locally be abundant in subduction mélanges (Cannaò et al., 2015) and subduction-related ophiolites (~ 5% in volume, Dai et al., 2016). Rodingites may also be relatively common in lithologically heterogeneous oceanic core complexes exhumed by detachment faulting at slow spreading centres (Boschi et al., 2006). At the present day, material produced at slow and ultra-slow spreading ridges is a minor portion of the oceanic lithosphere subducted globally (Alt et al., 2013), implying that a minimal amount of rodingites is currently subducted. However, these lithologies may have had greater impact in the Cretaceous and Cenozoic when the Jurassic Tethys oceanic lithosphere generated at slow and ultra-slow ridges subducted (e.g., Evans et al., 2017; Handy et al., 2010).

Thermodynamic modelling of the subduction evolution of metarodingites from Cerro del Almirez (Laborda-López et al., 2018) shows that these rocks underwent a P-T path similar to that of sub-arc domains in relatively hot and flat subduction zones (Syracuse et al., 2010) and remarkably similar to the average P-T conditions recorded by rocks exhumed from subduction zones (Penniston-Dorland et al., 2015). The geochemical evolution of the Cerro del Almirez metarodingites summarized in Figs. 11 and 12 can therefore assess the impact of these lithologies on the composition of fluids released in subduction zones and of crustal material recycled in the deep mantle.

5.7.1. Significance of metarodingites for the redox state of subduction zones

During progressive subduction before antigorite breakdown, dehydration reactions in serpentinites discharge fluids that oxidize iron in metarodingites (Fig. 11d). Fluids produced by incipient antigorite breakdown induce a similar effect (Laborda-López et al., 2018). Subducted metarodingites thus react with oxidizing fluids generated by dehydration reactions in serpentinites over a large range of pressure, and possibly limit the capacity of fluids to oxidize mantle wedge peridotites far from the slab (Debret and Sverjensky, 2017; Debret et al., 2015; Merkulova et al., 2017). Conversely, the formation of Pyrals-metarodingites and Chl-blackwalls in Chl-harzburgites occurs via reducing reactions (Fig. 12b) (Laborda-López et al., 2018) and may thus contribute to the redox budget of the deep sub-arc mantle (Evans, 2012) close to and beyond the P-T conditions of Atg breakdown. Moreover, metastable oxidized Grand- and Ep-metarodingites are preserved in the Chl-harzburgite domain as their complete transformation to Pyrals-metarodingites is kinetically inhibited (Laborda-López et al., 2018). Oxidized metastable metarodingites may thus subduct to the deep mantle and mix with the asthenosphere influencing its oxidation state.

5.7.2. Trace element partitioning into slab fluids

The mineral assemblages of metarodingites contain epidote minerals (allanite and epidote) during most of their subduction evolution up to ~ 2 GPa. These phases are the main repositories of LREE in metarodingites and preferentially partition these elements against fluids (Frei et al., 2004). Therefore, the presence of abundant metarodingites in the subducting slab may hinder the transfer of significant amounts of LREE to the mantle wedge. The stability of epidote in Ep-metarodingites also causes the incorporation of Sr, Pb and Ba (± Eu) from serpentinite-derived fluids (Fig. 12a). This effect is reverted at higher temperature when Ep-metarodingites convert to Pyrals-metarodingites (Fig. 12b) by, among other reactions, partial epidote breakdown to new

pyralspitic Grt-5. Ep-metarodingites may thus hamper the transfer of the Sr-Pb isotopic signatures of subducted lithologies to the source of arc magmas (Fig. 12e) and incorporate Sr-Pb from dehydrating metasedimentary rocks more efficiently than ultramafic rocks (Cannaò et al., 2015). Moreover, the partitioning of Ba into epidote of metarodingites may generate slab fluids with low Ba/Th and Ba/Nb ratios that mimic the geochemical imprint of melt from subducted sediments in the sub-arc mantle (Elliott et al., 1997). Therefore, the application of trace element ratios in arc lavas to identify the subduction components in their sources (e.g., Pearce et al., 2005) should take into account the effect of element fractionation by minerals in the slab rocks, including metarodingites.

5.7.3. Lithological heterogeneity at the slab-mantle interface

Similar to metasedimentary and other metamafic rocks, subducted metarodingites and spatially-related reaction rims may experience tectonic and metasomatic mixing at the slab-mantle interface (Fig. 12e) (e.g., Bebout and Barton, 2002; Bebout and Penniston-Dorland, 2016; Gorman et al., 2018; Penniston-Dorland et al., 2012, 2014; Schwarzenbach et al., 2018). Indeed, PGE abundances and Os isotopes indicate local mass transfer between metarodingites and metasomatic rims likely favoured by the weak rheology of the latter (see section 5.2.). Fluid-mediated mass transfer and metasomatic alteration caused by juxtaposition of disparate lithologies in subduction mélanges may generate hybrid domains with the trace element and isotopic signatures of arc magmas (e.g., Bebout and Barton, 2002; Spandler et al., 2008). These domains may then rise in buoyant diapirs toward the inner and hotter region of the mantle wedge and produce magmas with subduction-related affinity (Marschall and Schumacher, 2012).

Despite their limited thickness at Cerro del Almirez, Chl-blackwalls formed by metasomatic reactions at the metarodingite-serpentinite interface (Fig. 11c, d) illustrate an example of the potential impact of metarodingites on the transfer of trace elements at the slab-mantle interface. These lithologies are dominated by chlorite and are so similar to chlorite schists present in high-pressure subduction mélanges (Spandler et al., 2008). Owing to the high stability of chlorite in this type of rocks (Bebout, 1991), Chl-blackwalls around metarodingite bodies may be important carriers of volatiles in the deep mantle, especially beyond the stability field of serpentine, and may liberate fluids able to leach trace elements from metasedimentary and mafic rocks. Therefore, metarodingites and associated metasomatic rims, which can metastably persist beyond their stability fields in the slab (Laborda-López et al., 2018), are additional lithologies that should be considered in models of trace element mobility in deep subduction mélanges (Fig. 12e).

5.7.4. Mobility of rhenium

Metarodingites from Cerro del Almirez underwent loss of Re during subduction (Fig. 11d), probably favoured by the relatively oxidizing nature of fluids produced by serpentinite dehydration (Reisberg et al., 2008). The redox signature of fluids liberated from subducting serpentinites is linked to the extent of serpentinization of their mantle precursors (Evans et al., 2017). Extensive serpentinization at the seafloor of hyperextended continental margins (Fig. 11a) or ultra-slow spreading centres induces the release of oxidizing fluids by serpentinite dehydration at high pressure (Debret and Sverjensky, 2017; Evans et al., 2017). Therefore, subduction of metarodingites from magma-poor tectonic settings may promote rhenium endowment in the supra-subduction mantle by transport of Re in serpentinite-derived oxidizing fluids. Enrichment of supra-subduction peridotites in Re from slab eclogites (Dale et al., 2009)

and metarodingites (this work) may generate arc magmas relatively rich in this metal, and explain the radiogenic $^{187}Os/^{188}Os$ signature of some arc lavas and arc mantle xenoliths (Gannoun et al., 2016), which implies relatively high time-integrated Re/Os ratios.

5.7.5. Calcium recycling in subduction zones

An important influence of metarodingites on the composition of fluids liberated by subducting slabs is to enhance their Ca concentrations. Metarodingites incorporate Ca mainly from abyssal serpentinites on the seafloor, and they are notably richer in Ca than other high-pressure metamafic rocks (i.e., common blueschists and eclogites). However, up to half of the whole-rock Ca budget of metarodingites (Fig. 2a) can be released in fluids upon subduction at the P-T conditions of Grand-Ep (Fig. 12a) and Ep-Pyrals metarodingite transitions (Fig. 12b), thus possibly endowing sub-arc mantle peridotites with Ca (Fig. 12e).

Despite their important Ca loss during subduction, metarodingites subducted to ~ 2 GPa are still richer in calcium than metamafic rocks with MORB-like compositions (Fig. 2a). Moreover, metastable Ca-rich Grand- and Ep-metarodingites may subduct to higher depths than those corresponding to their transformation to Ca-poorer Pyrals-metarodingites, as this reaction is hampered by the strong rheology and low permeability of metarodingites (Laborda-López et al., 2018). Crystallization of Ca-rich minerals in polyphase inclusions in diamond from 300-360 km depths has been ascribed to subduction and recycling of crustal Ca-rich lithologies in the convective upper mantle (Brenker et al., 2005). Metarodingites, ophicarbonates, and calcareous-siliceous oozes are plausible sources of this calcium-silicate reservoir in the deep mantle (Brenker et al., 2005). Subduction and recycling of Ca-rich metarodingites in the asthenosphere (Fig.

12e) may therefore generate a deep Ca-rich reservoir with some of the geochemical characteristics of ocean island basalts (OIB) (Brenker et al., 2005).

6. CONCLUSIONS

Metarodingites from Cerro del Almirez derive from basalts and dolerites that experienced loss of Si, Na, LILE (K, Cs, Rb, Ba, Sr) and Pb and enrichment of Ca caused by rodingitization concomitant with serpentinization of host peridotites close to the seafloor (Fig. 11c). During rodingitization, REE remained immobile at the whole-rock scale and partitioned between the new metamorphic minerals, HREE mostly into granditic Grt-1. At the seafloor and during subduction, strong gradients of chemical potentials of Mg, Ca and Al at the rodingite-serpentinite interface caused the heterogeneous transformation of rodingite rim into Chl-blackwall and of serpentinite into Chl-Di and Chl-Ol-Di-metasomatic rinds (Fig. 11c, d).

Metarodingites and metasomatic reaction rims locally exchanged PGE by fluid advection and subduction shearing favoured by the abundance of weak chlorite at their contact. Prograde subduction metamorphism induced iron oxidation and Re loss in Grand-metarodingites, associated with partial replacement of Grt-1 by more andraditic Grt-2 and Grt-3 with higher MREE/HREE ratios (Fig. 11d). Accessory allanite efficiently sequestered LREE and Th in subducting Grand-metarodingites up to ~ 2 GPa.

Due to the intense flux of relatively oxidizing fluids produced by the antigorite breakdown in host serpentinites, Grand-metarodingites transformed into Ep-metarodingites causing the liberation of Ca and Mn in fluids and the capture of Si, Sr, Pb, Ba and Eu mostly into epidote (Fig. 12a). At peak metamorphic conditions, Ep-metarodingites transformed into Pyrals-metarodingites by reducing reactions that consumed epidote and released Ca, Sr and Pb beyond the conditions of antigorite

breakdown in serpentinites (Fig. 12b). All metarodingite types experienced late amphibolitization triggered by incoming external fluids from metasedimentary rocks that caused enrichment in Mg, Fe^{2+}, Na, K, Cs, Rb, Ba and depletion in Ca and Fe^{3+} (Fig. 12c).

Metarodingites in subducting slab and at the slab-mantle interface may reduce the oxidizing capacity of serpentinite-derived fluids and, if recycled by deep subduction, affect the redox budget of the convective mantle. Allanite and epidote in metarodingites act as sinks of LREE-Th and Sr-Pb-Ba, respectively, and concur to hold these elements in the subducting slab. This retention may hinder the identification of the slab component (e.g., fluid from the mafic crust vs. melt from metasedimentary rocks) and the quantification of its imprint in the sources of arc magmas. Metarodingites and related metasomatic rims contribute to the lithological and compositional heterogeneity of the slab-mantle interface and influence the mobility of trace elements in this crucial region of subduction zones. The release of Ca and Re from metarodingites in slab fluids may induce metasomatism in the sub-arc mantle. However, subducted metarodingites still preserve an important part of their Ca budgets at eclogite facies conditions and their recycling in the deep asthenosphere may generate Ca-rich reservoirs.

ACKNOWLEDGEMENTS

We thank Sarah C. Penniston-Dorland and Gisella Rebay for their constructive reviews of the submitted version of the manuscript. The Sierra Nevada National Park is acknowledged for providing permits for fieldwork and sampling. Research leading to these results was funded by C.L.L.'s Ph.D. project BES-2013-065336, by grants no. CGL2012-32067, CGL2015-71692-P and CGL2016-75224-R from the Spanish "Ministerio de Economía, Industria y Competitividad" (MINECO), and "Junta de Andalucía" research groups RNM-145, RNM-148 and RNM-374, and grant P12-RNM-

3141. C.M. acknowledges funding by Ramón y Cajal fellowship RYC-2012-11314 and grant no. CGL2016-81085-R from MINECO, and "Junta de Andalucía" grant B-RNM-189-UGR18 and research group RNM-131. Research grants, infrastructures and human resources leading to this research have benefited from funding by the European Social Fund and the European Regional Development Fund.

FIGURE CAPTIONS

Figure 1. a) Geological sketch map of the Nevado-Filábride Complex in the Betic Cordillera (modified from Jabaloy-Sánchez et al., 2015) with the location of the Cerro del Almirez ultramafic massif (yellow box) shown in (b). The inset displays the main geological units of the westernmost Mediterranean. b) Geological map of the Cerro del Almirez area with the location of the sampled metarodingite bodies. The colours of circles indicate the metarodingite type (± amphibolitized). c) Schematic lithostratigraphic section of the Cerro del Almirez ultramafic massif with the different types of metarodingite. Not to scale. Same colour key for metarodingite types and host ultramafic rocks as in (b). Grey edges represent the metasomatic reaction rims altogether. Modified from Laborda-López et al. (2018).

Figure 2. Whole-rock abundances of SiO_2 versus CaO (a), MgO versus CaO (b) and Al_2O_3 versus $Na_2O + K_2O$ (c) of the Cerro del Almirez metarodingites. All data on anhydrous basis in wt.%. Red circles = Grandite (Grand)-metarodingites; yellow circles = Epidote (Ep)-metarodingites; blue circles = Pyralspite (Pyrals)-metarodingites; green ring = amphibolitized samples. Compositional fields of metarodingites from other locations are plotted in (a) for comparison: pink area = vesuvianite-rich rodingites; red area = grandite-rich rodingites; yellow area = epidote-rich rodingites (data from Attoh et al., 2006; Früh-Green et al., 2017; Fukuyama et al., 2014; Koutsovitis et al., 2013; Li et al., 2004, 2017; Panseri et al., 2008); light blue area = pyralspite-rich metarodingites

from Cima di Gagnone (Evans et al., 1979, 1981). The dark blue field represents the compositions of common MORB (Jenner and O´Neill, 2012), the brown area the compositions of ocean-continent transition (OCT) basalts (Desmurs et al., 2002), the purple area the compositions of metamafic (non-rodingitized) rocks from the Nevado-Filábride Complex (NFC) (Gómez-Pugnaire et al., 2000, and references therein; Puga et al., 2011, and references therein). The compositional variations of chlorite (Chl)-blackwalls (grey triangles), chlorite-diopside (Di)- and chlorite-olivine (Ol)-diopside-metasomatic rims (white inverse triangles), and host ultramafic rocks (green area) are also shown in (b).

Figure 3. Whole-rock abundances of Fe_2O_3 versus FeO (a) and SiO_2 versus Al_2O_3 (b) in metarodingites, metasomatic reaction rims and host ultramafic rocks from Cerro del Almirez. All data on anhydrous basis in wt.%. Metarodingite symbols in (a) as in Fig. 2. Panel (a) also shows the compositional fields of Chl-blackwalls around metarodingites in the Atg-serpentinite (light grey area) and Chl-harzburgite domains (dark grey area), Chl-Di- and Chl-Ol-Di-metasomatic rims (yellow area), Atg-serpentinites (green area), transitional Chl-serpentinites and Atg-Chl-Opx-Ol rocks at the dehydration front (blue area), and Chl-harzburgites (brownish orange area). The red arrow in (a) represents the trend due to increasing abundances of andradite (Fe^{3+})-rich garnets (Grt-2 and Grt-3) in Grand-metarodingites. In (b), symbols of Chl-blackwalls, Chl-Di- and Chl-Ol-Di metasomatic rims are as in Fig. 2, green squares represent Atg-serpentinites, blue hexagons represent transitional Chl-serpentinites and Atg-Chl-Opx-Ol rocks, and brownish orange diamonds represent Chl-harzburgites hosting metarodingites. Metarodingite compositional field (red area) is also plotted for comparison in (b).

Figure 4. Chondrite-normalized REE patterns of metarodingites (a), metasomatic reaction rims (b), Atg-serpentinites and transitional Chl-serpentinites and Atg-Chl-Opx-

Ol rocks (c), and Chl-harzburgites (d) from Cerro del Almirez. Normalizing values from Anders and Grevesse (1989). Symbols as in Figs. 2 and 3. E-MORB (brown line) and N-MORB (blue line) compositions are from Klein (2003). Representative composition of ocean-continent transition (OCT) basalt (pink line) from the Platta Nappe is from Desmurs et al. (2002). The purple area represents the REE variations of the Nevado-Filábride Complex (NFC) (non-rodingitized) metamafic rocks. In (b), the compositions of metarodingites (red area) and host ultramafic rocks (green area) are plotted for comparison, as well as the compositions of Atg-serpentinites (green area) in (d).

Figure 5. Primitive upper mantle (PUM)-normalized trace element patterns of metarodingites (a), metasomatic reaction rims (b), Atg-serpentinites and transitional Chl-serpentinites and Atg-Chl-Opx-Ol rocks (c), and Chl-harzburgites (d) from Cerro del Almirez. Normalizing values from Sun and McDonough (1989). Symbols and sources of reference compositions as in Figs. 2, 3 and 4. The yellow area in (c) represents the compositions of Chl-Di- and Chl-Ol-Di-metasomatic rims.

Figure 6. Chondrite-normalized REE patterns (a) and primitive upper mantle (PUM)-normalized trace element patterns (b) of the different types of garnet in the Cerro del Almirez metarodingites. Normalizing values from Anders and Grevesse (1989) and Sun and McDonough (1989). Brown, pink and green areas mark the compositional variations of Grt-1, Grt-2 and Grt-3 in Grand-metarodingites, respectively. Red and orange circles indicate the compositions of Grt-2 and new Grt-4 in Ep-metarodingites, respectively. Blue circles indicate the compositions of Grt-5 in Pyrals-metarodingites.

Figure 7. Chondrite-normalized REE patterns (a) and primitive upper mantle (PUM)-normalized trace element patterns (b) of allanite and epidote in the Almirez metarodingites. Normalizing values from Anders and Grevesse (1989) and Sun and McDonough (1989). Brown squares and area indicate the composition of allanite in

Grand-metarodingites. Yellow squares and circles mark the compositions of epidote in Ep-metarodingites from the Atg-serpentinite and Chl-harzburgite domains, respectively. Dotted yellow circles mark the compositions of epidote in Pyrals-metarodingites.

Figure 8. Chondrite-normalized REE patterns (a) and primitive upper mantle (PUM)-normalized trace element patterns (b) of diopside and pargasitic amphibole (Amp-2) in the Cerro del Almirez metarodingites. Normalizing values from Anders and Grevesse (1989) and Sun and McDonough (1989). Orange and yellow squares indicate the compositions of diopside in Grand- and Ep-metarodingites, respectively. Blue circles indicate the compositions of diopside in Pyrals-metarodingites. Green and grey areas mark the compositional variations of Amp-2 in Grand- and Pyrals-metarodingites, respectively.

Figure 9. Primitive upper mantle (PUM)-normalized PGE-Re patterns of metarodingites (a), Chl-blackwalls and Chl-(± Ol-)Di-metasomatic rims (b), host Atg-serpentinites (c) and Chl-harzburgites (d) from Cerro del Almirez. Normalizing values from Becker et al. (2006). Symbols as in Figs. 2 and 3. PGE-Re compositions of MORB (grey field) in (a) and (b) is from Gannoun et al. (2016), and references therein. Depleted MORB mantle (DMM) composition in (b), (c) and (d) (red dashed line) is from Salters and Stracke (2004).

Figure 10. Os concentrations (ppb) versus present-day $^{187}Os/^{188}Os$ in metarodingites, Chl-blackwalls, Chl-(± Ol-)Di-metasomatic rims, and host Atg-serpentinites and Chl-harzburgites from Cerro del Almirez. Symbols as in Figs. 2 and 3.

Figure 11. a) Geological sketch of the Mesozoic ocean-continent transition zone (OCT) in which serpentinites and rodingites from Cerro del Almirez may have formed on the seafloor. b) Detailed representation of oceanic serpentinization of exhumed mantle peridotites and rodingitization of mafic dykes by percolation of reducing fluids (pink

arrows). c) Cartoon illustrating the generation of Grand-rodingites and metasomatic reaction rims on the seafloor (rodingitization). Light yellow spots symbolize diopside grains. Pink arrows represent fluidspromoting element exchanges between ultramafic and mafic rocks during rodingitization, and purple arrows the subsequent diffusion of Mg, Ca and Al between rodingite and serpentinite forming the metasomatic rims. d) Sketch of structural and chemical processes triggered by prograde metamorphism in Grand-metarodingites prior to Atg-breakdown in the host serpentinites. Red arrows: relatively oxidant fluids.

Figure 12. a) Sketch showing the mineralogical and compositional changes associated with transformation of Grand- to Ep-metarodingites triggered by fluids liberated through dehydration of Atg-serpentinites to Chl-harzburgites. Red arrows: relatively oxidant serpentinite-derived fluids. b) Cartoon resuming the compositional changes related to transformation of Ep- to Pyrals-metarodingites at peak metamorphic conditions in the Chl-harzburgite stability field. c) Sketch of the mineralogical and geochemical modifications due to late amphibolitization of metarodingites. d) Geological sketch representing the proposed setting of the Cerro del Almirez ultramafic massif (black box) during the Miocene subduction of the Nevado-Filábride Complex. e) Schematic representation of the main geochemical exchanges (thick pink arrows) at the slab-mantle interface caused by the presence of metarodingites fluxed by fluids from dehydrating serpentinites (red arrows).

Figure S1. Whole-rock abundances of Nb versus Ce (a) and Pr (b), and of V versus Yb (c) and Lu (d) of the Cerro del Almirez metarodingites. All data in ppm. Red circles = Grandite (Grand)-metarodingites; yellow circles = Epidote (Ep)-metarodingites; blue circles = Pyralspite (Pyrals)-metarodingites; green ring = amphibolitized samples.

REFERENCES

Allen, D.E., Seyfried Jr, W.E., 2005. REE controls in ultramafic hosted MOR hydrothermal systems: an experimental study at elevated temperature and pressure. Geochimica et Cosmochimica Acta, 69(3): 675-683.

Alt, J.C., Garrido, C.J., Shanks III, W.C., Turchyn, A., Padrón-Navarta, J.A., López Sánchez-Vizcaíno, V., Gómez Pugnaire, M.T., Marchesi, C.,2012. Recycling of water, carbon, and sulfur during subduction of serpentinites: A stable isotope study of Cerro del Almirez, Spain. Earth and Planetary Science Letters, 327-328: 50-60.

Alt, J.C., Schwarzenbach, E.M., Früh-Green, G.L., Shanks III, W.C., Bernasconi, S.M., Garrido, C.J., Crispini, L., Gaggero, L., Padrón-Navarta, J.A., Marchesi, C., 2013. The role of serpentinites in cycling of carbon and sulfur: Seafloor serpentinization and subduction metamorphism. Lithos, 178: 40-54.

Anders, E., Grevesse, N., 1989. Abundances of the elements: Meteoritic and solar. Geochimica et Cosmochimica Acta, 53(1): 197-214.

Attoh, K., Evans, M.J., Bickford, M.E., 2006. Geochemistry of an ultramafic-rodingite rock association in the Paleoproterozoic Dixcove greenstone belt, southwestern Ghana. Journal of African Earth Sciences, 45(3): 333-346.

Austrheim, H., Prestvik, T., 2008. Rodingitization and hydration of the oceanic lithosphere as developed in the Leka ophiolite, north–central Norway. Lithos, 104: 177-198.

Bach, W., Klein, F., 2009. The petrology of seafloor rodingites: Insights from geochemical reaction path modeling. Lithos, 112(1-2): 103-117.

Beard, J.S., Fullagar, P.D., Krishna Sinha, A., 2002. Gabbroic pegmatite intrusions, Iberia Abyssal Plain, ODP Leg 173, Site 1070: magmatism during a transition from non-volcanic rifting to sea-floor spreading. Journal of Petrology, 43(5): 885-905.

Bebout, G.E., 1991. Field-based evidence for devolatilization in subduction zones: implications for arc magmatism. Science, 251(4992): 413-416.

Bebout, G.E., 2014. Chemical and isotopic cycling in subduction zones, in: Holland, H.D., Turekian, K.K. (Eds.), Treatise on Geochemistry, vol. 4. The Crust. Elsevier, pp. 703-747.

Bebout, G.E., Barton, M.D., 2002. Tectonic and metasomatic mixing in a high-T, subduction-zone mélange—insights into the geochemical evolution of the slab–mantle interface. Chemical Geology, 187(1-2): 79-106.

Bebout, G.E., Penniston-Dorland, S.C., 2016. Fluid and mass transfer at subduction interfaces—The field metamorphic record. Lithos, 240-243: 228-258.

Becker, H., 2000. Re–Os fractionation in eclogites and blueschists and the implications for recycling of oceanic crust into the mantle. Earth and Planetary Science Letters, 177(3-4): 287-300.

Becker, H., Horan, M.F., Walker, R.J., Gao, S., Lorand, J.-P., Rudnick, R.L., 2006. Highly siderophile element composition of the Earth's primitive upper mantle: Constraints from new data on peridotite massifs and xenoliths. Geochimica et Cosmochimica Acta, 70: 4528-4550.

Boschi, C., Früh-Green, G.L., Delacour, A., Karson, J.A., Kelley, D.S., 2006. Mass transfer and fluid flow during detachment faulting and development of an oceanic core complex, Atlantis Massif (MAR 30°N). Geochemistry, Geophysics, Geosystems, 7(1): Q01004. DOI:10.1029/2005GC001074

Brenker, F.E., Vincze, L., Vekemans, B., Nasdala, L., Stachel, T., Vollmer, C., Kersten, M., Somogyi, A., Adams, F., Joswig W., Harris, J.W., 2005. Detection of a Ca-rich lithology in the Earth's deep (> 300 km) convecting mantle. Earth and Planetary Science Letters, 236(3-4): 579-587.

Bretscher, A., Hermann, J., Pettke, T., 2018. The influence of oceanic oxidation on serpentinite dehydration during subduction. Earth and Planetary Science Letters, 499: 173-184.

Cannaò, E., Agostini, S., Scambelluri, M., Tonarini, S., Godard, M., 2015. B, Sr and Pb isotope geochemistry of high-pressure Alpine metaperidotites monitors fluid-mediated element recycling during serpentinite dehydration in subduction mélange (Cima di Gagnone, Swiss Central Alps). Geochimica et Cosmochimica Acta, 163: 80-100.

Coleman, R.G., 1967. Low-temperature reaction zones and alpine ultramafic rocks of California, Oregon, and Washington. United States Geological Survey Bulletin, 1247: 49 pp.

Dai, J.G., Wang, C.S., Liu, S.A., Qian, X.Y., Zhu, D.C., Ke, S., 2016. Deep carbon cycle recorded by calcium-silicate rocks (rodingites) in a subduction-related ophiolite. Geophysical Research Letters, 43(22): 11635-11643.

Dale, C.W., Gannoun, A., Burton, K.W., Argles, T.W., Parkinson, I.J., 2007. Rhenium–osmium isotope and elemental behaviour during subduction of oceanic crust and

the implications for mantle recycling. Earth and Planetary Science Letters, 253(1-2): 211-225.

Dale, C.W., Burton, K.W., Pearson, D.G., Gannoun, A., Alard, O., Argles, T.W., Parkinson, I.J., 2009. Highly siderophile element behaviour accompanying subduction of oceanic crust: whole rock and mineral-scale insights from a high-pressure terrain. Geochimica et Cosmochimica Acta, 73(5): 1394-1416.

Debret, B., Sverjensky, D.A., 2017. Highly oxidising fluids generated during serpentinite breakdown in subduction zones. Scientific Reports 7, 10351. DOI:10310.11038/s41598-10017-09626-y

Debret, B., Bolfan-Casanova, N., Padrón-Navarta, J.A., Martin-Hernández, F., Andreani, M., Garrido, C.J., López Sánchez-Vizcaíno, V., Gómez-Pugnaire, M.T., Muñoz, M., Trcera, N.2015. Redox state of iron during high-pressure serpentinite dehydration. Contributions to Mineralogy and Petrology, 169(4): 36. DOI 10.1007/s00410-015-1130-y

Desmurs, L., Müntener, O., Manatschal, G., 2002. Onset of magmatic accretion within a magma-poor rifted margin: a case study from the Platta ocean-continent transition, eastern Switzerland. Contributions to Mineralogy and Petrology, 144(3): 365-382.

Elliott, T., Plank, T., Zindler, A., White, W., Bourdon, B., 1997. Element transport from slab to volcanic front at the Mariana arc. Journal of Geophysical Research: Solid Earth, 102(B7): 14991-15019.

Evans, B.W., Trommsdorff, V., Richter, W., 1979. Petrology of an eclogite-metarodingite suite at Cima di Gagnone, Ticino, Switzerland. American Mineralogist, 64(1-2): 15-31.

Evans, B.W., Trommsdorff, V., Goles, G.G., 1981. Geochemistry of high-grade eclogites and metarodingites from the Central Alps. Contributions to Mineralogy and Petrology, 76(3): 301-311.

Evans, K.A., 2012. The redox budget of subduction zones. Earth-Science Reviews, 113(1-2): 11-32.

Evans, K.A., Reddy, S.M., Tomkins, A.G., Crossley, R.J., Frost, B.R., 2017. Effects of geodynamic setting on the redox state of fluids released by subducted mantle lithosphere. Lithos, 278-281: 26-42.

Frei, D., Liebscher, A., Franz, G., Dulski, P., 2004. Trace element geochemistry of epidote minerals. Reviews in Mineralogy and Geochemistry, 56(1): 553-605.

Frost, B.R., Beard, J.S., 2007. On silica activity and serpentinization. Journal of Petrology, 48(7): 1351-1368.

Frost, B.R., Beard, J.S., McCaig, A., Condliffe, E., 2008. The formation of micro-rodingites from IODP Hole U1309D: key to understanding the process of serpentinization. Journal of Petrology, 49(9): 1579-1588.

Früh-Green, G.L., Orcutt, B.N., Green, S.L., Cotterill, C., and the Expedition 357 Scientists, 2017. Expedition 357 summary. Proceedings of the International Ocean Discovery Program, 357: 34 pp. DOI:10.14379/iodp.proc.357.101.2017

Fukuyama, M., Ogasawara, M., Dunkley, D.J., Wang, K.-L., Lee, D.-C., Hokada, T., Maki, K., Hirata, T., Kon, Y., 2014. The formation of rodingite in the Nagasaki metamorphic rocks at Nomo Peninsula, Kyushu, Japan–Zircon U–Pb and Hf isotopes and trace element evidence. Island Arc, 23(4): 281-298.

Gannoun, A., Burton, K.W., Day, J.M.D., Harvey, J., Schiano, P., Parkinson, I., 2016. Highly siderophile element and Os isotope systematics of volcanic rocks at divergent and convergent plate boundaries and in intraplate settings. Reviews in Mineralogy and Geochemistry, 81(1): 451-724.

Garrido, C.J., López Sánchez-Vizcaíno, V., Gómez Pugnaire, M.T., Trommsdorff, V., Alard, O., Bodinier, J—L., Godard, M., 2005. Enrichment of HFSE in chlorite-harzburgite produced by high-pressure dehydration of antigorite-serpentinite: implications for subduction magmatism. Geochemistry, Geophysics, Geosystems, 6(1): Q01J15. DOI:10.1029/2004GC000791

Gaspar, M., Knaack, C., Meinert, L.D., Moretti, R., 2008. REE in skarn systems: A LA-ICP-MS study of garnets from the Crown Jewel gold deposit. Geochimica et Cosmochimica Acta, 72(1): 185-205.

Gómez-Pugnaire, M.T., Ulmer, P., López-Sánchez-Vizcaíno, V., 2000. Petrogenesis of the mafic igneous rocks of the Betic Cordilleras: A field, petrological and geochemical study. Contributions to Mineralogy and Petrology, 139(4): 436-457.

Gómez-Pugnaire, M.T., Rubatto, D., Fernández-Soler, J.M., Jabaloy, A., López Sánchez-Vizcaíno, V., González-Lodeiro, F., Galindo-Zaldívar, J., Padrón-Navarta, J.A., 2012. Late Variscan magmatism in the Nevado-Filábride Complex: U-Pb geochronologic evidence for the pre-Mesozoic nature of the deepest Betic complex (SE Spain). Lithos, 146-147: 93-111.

Gómez-Pugnaire, M.T., Nieto, F., Abad, I., Velilla, N., Garrido, C.J., Acosta-Vigil, A., Barich, A., Hidas, K., López Sánchez-Vizcaíno, V., 2019. Alpine Metamorphism in the Betic Internal Zones. The Geology of Iberia: A Geodynamic Approach. Springer, pp. 519-544.

Gorman, J.K., Penniston-Dorland, S.C., Marschall, H.R., Walker, R.J., 2019. The roles of mechanical mixing and fluid transport in the formation of reaction zones in subduction-related mélange: Evidence from highly siderophile elements. Chemical Geology, 525: 96-111.

Haas, J.R., Shock, E.L., Sassani, D.C., 1995. Rare earth elements in hydrothermal systems: estimates of standard partial molal thermodynamic properties of aqueous complexes of the rare earth elements at high pressures and temperatures. Geochimica et Cosmochimica Acta, 59(21): 4329-4350.

Hacker, B.R., Abers, G.A., Peacock, S.M., 2003. Subduction factory 1. Theoretical mineralogy, densities, seismic wave speeds, and H_2O contents. Journal of Geophysical Research: Solid Earth, 108(B1). DOI:10.1029/2001JB001127

Handy, M.R., Schmid, S.M., Bousquet, R., Kissling, E., Bernoulli, D., 2010. Reconciling plate-tectonic reconstructions of Alpine Tethys with the geological–geophysical record of spreading and subduction in the Alps. Earth-Science Reviews, 102(3-4): 121-158.

Hermann, J., 2002. Allanite: thorium and light rare earth element carrier in subducted crust. Chemical Geology, 192(3-4): 289-306.

Hu, C.-N., Santosh, M., Yang, Q.-Y., Kim, S.W., Nakagawa, M., Maruyama, S., 2017. Magmatic and metasomatic imprints in a long-lasting subduction zone: evidence from zircon in rodingite and serpentinite of Kochi, SW Japan. Lithos, 274-275: 349-362.

Ishimaru, S., Arai, S., 2011. Peculiar Mg–Ca–Si metasomatism along a shear zone within the mantle wedge: inference from fine-grained xenoliths from Avacha volcano, Kamchatka. Contributions to Mineralogy and Petrology, 161(5): 703-720.

Jabaloy-Sánchez, A., Gómez-Pugnaire, M.T., Padrón-Navarta, J.A., López Sánchez-Vizcaíno, V., Garrido, C.J., 2015. Subduction- and exhumation-related structures preserved in metaserpentinites and associated metasediments from the Nevado–Filábride Complex (Betic Cordillera, SE Spain). Tectonophysics, 644-645: 40-57.

Jabaloy-Sánchez, A., Talavera, C., Gómez-Pugnaire, M.T., López Sánchez-Vizcaíno, V., Vázquez-Vílchez, M., Rodríguez-Peces, M.J., Evans, N.J., 2018. U-Pb ages of detrital zircons from the Internal Betics: A key to deciphering paleogeographic provenance and tectono-stratigraphic evolution. Lithos, 318-319: 244-266.

Jenner, F.E., O'Neill, H.S.C., 2012. Analysis of 60 elements in 616 ocean floor basaltic glasses. Geochemistry, Geophysics, Geosystems, 13(1): Q02005. DOI:10.1029/2011GC004009

Kelemen, P.B., Hanghøj, K., Greene, A.R., 2014. One view of the geochemistry of subduction-related magmatic arcs, with an emphasis on primitive andesite and lower crust. In: Holland, H.D., Turekian, K.K. (Eds.), Treatise on Geochemistry, vol. 4. The Crust. Elsevier, pp. 749-806.

Kendrick, M.A., Scambelluri, M., Honda, M., Phillips, D., 2011. High abundances of noble gas and chlorine delivered to the mantle by serpentinite subduction. Nature Geoscience, 4(11): 807-812.

Kirchner, K.L., Behr, W.M., Loewy, S., Stockli, D.F., 2016. Early Miocene subduction in the western Mediterranean: Constraints from Rb-Sr multimineral isochron geochronology. Geochemistry, Geophysics, Geosystems, 17(5): 1842-1860.

Klein, E.M., 2003. Geochemistry of the igneous oceanic crust. In: Holland, H.D., Turekian, K.K. (Eds.), Treatise on Geochemistry, vol. 3. The Crust. Elsevier, pp. 433-463.

Koutsovitis, P., Magganas, A., Pomonis, P., Ntaflos, T., 2013. Subduction-related rodingites from East Othris, Greece: Mineral reactions and physicochemical conditions of formation. Lithos, 172-173: 139-157.

Koutsovitis, P., Magganas, A., Ntaflos, T., Koukouzas, N., 2018. Rodingitization and carbonation, associated with serpentinization of Triassic ultramafic cumulates and lavas in Othris, Greece. Lithos, 320-321: 35-48.

Laborda-López, C., López Sánchez-Vizcaíno, V., Marchesi, C., Gómez-Pugnaire, M.T., Garrido, C.J., Jabaloy-Sánchez, A., Padrón-Navarta, J.A., Hidas, K., 2018. High-P metamorphism of rodingites during serpentinite dehydration (Cerro del Almirez, Southern Spain): Implications for the redox state in subduction zones. Journal of Metamorphic Geology, 36(9): 1141-1173.

Li, X.-P., Rahn, M., Bucher, K., 2004. Metamorphic processes in rodingites of the Zermatt-Saas ophiolites. International Geology Review, 46(1): 28-51.

Li, X.-P., Zhang, L., Wei, C., Ai, Y., Chen, J., 2007. Petrology of rodingite derived from eclogite in western Tianshan, China. Journal of Metamorphic Geology, 25(3): 363-382.

Li, X.-P., Duan, W.-Y., Zhao, L.-Q., Schertl, H.-P., Kong, F.-M., Shi, T.-Q., Zhang, X., 2017. Rodingites from the Xigaze ophiolite, southern Tibet – new insights into the processes of rodingitization. European Journal of Mineralogy, 29: 821-837.

Loader, M.A., Wilkinson, J.J., Armstrong, R.N., 2017. The effect of titanite crystallisation on Eu and Ce anomalies in zircon and its implications for the assessment of porphyry Cu deposit fertility. Earth and Planetary Science Letters, 472: 107-119.

López Sánchez-Vizcaíno, V., Rubatto, D., Gómez-Pugnaire, M.T., Trommsdorff, V., Müntener, O., 2001. Middle Miocene high-pressure metamorphism and fast exhumation of the Nevado-Filábride Complex, SE Spain. Terra Nova, 13(5): 327-332.

López Sánchez-Vizcaíno, V., Trommsdorff, V., Gómez-Pugnaire, M.T., Garrido, C.J., Müntener, O, Connolly, J.A.D., 2005. Petrology of titanian clinohumite and olivine at the high-pressure breakdown of antigorite serpentinite to chlorite harzburgite (Almirez Massif, S. Spain). Contributions to Mineralogy and Petrology, 149(6): 627-646.

López Sánchez-Vizcaíno, V., Gómez-Pugnaire, M.T., Garrido, C.J., Padrón-Navarta, J.A., Mellini, M., 2009. Breakdown mechanisms of titanclinohumite in antigorite serpentinite (Cerro del Almirez massif, S. Spain): A petrological and TEM study. Lithos, 107(3): 216-226.

Manatschal, G., Müntener, O., 2009. A type sequence across an ancient magma-poor ocean–continent transition: the example of the western Alpine Tethys ophiolites. Tectonophysics, 473(1-2): 4-19.

Marchesi, C., Garrido, C.J., Padrón-Navarta, J.A., López Sánchez-Vizcaíno, V., Gómez-Pugnaire, M.T., 2013. Element mobility from seafloor serpentinization to high-pressure dehydration of antigorite in subducted serpentinite: insights from the Cerro del Almirez ultramafic massif (southern Spain). Lithos, 178: 128-142.

Marks, M.A.W., Coulson, I.M., Schilling, J., Jacob, D.E., Schmitt, A.K., Markl, G., 2008. The effect of titanite and other HFSE-rich mineral (Ti-bearing andradite,

zircon, eudialyte) fractionation on the geochemical evolution of silicate melts. Chemical Geology, 257(1-2): 153-172.

Marschall, H.R., Schumacher, J.C., 2012. Arc magmas sourced from mélange diapirs in subduction zones. Nature Geoscience, 5: 862–867.

Marschall, H.R., Altherr, R., Ludwig, T., Kalt, A., Gméling, K., Kasztovszky, Z., 2006. Partitioning and budget of Li, Be and B in high-pressure metamorphic rocks. Geochimica et Cosmochimica Acta, 70(18): 4750-4769.

McInnes, B.I.A., McBride, J.S., Evans, N.J., Lambert, D.D., Andrew, A.S., 1999. Osmium isotope constraints on ore metal recycling in subduction zones. Science, 286(5439): 512-516.

Merkulova, M.V., Muñoz, M., Brunet, F., Vidal, O., Hattori, K., Vantelon, D., Trcera, N., Huthwelker, T., 2017. Experimental insight into redox transfer by iron- and sulfur-bearing serpentinite dehydration in subduction zones. Earth and Planetary Science Letters, 479: 133-143.

Niu, Y., 2004. Bulk-rock major and trace element compositions of abyssal peridotites: implications for mantle melting, melt extraction and post-melting processes beneath mid-ocean ridges. Journal of Petrology, 45(12): 2423-2458.

Padrón Navarta, J.A., Hermann, J., López Sánchez-Vizcaíno, V., Garrido, C.J., Gómez-Pugnaire, M.T., 2010a. An experimental investigation of antigorite dehydration in natural silica-enriched serpentinite. Contributions to Mineralogy and Petrology, 159: 25-42.

Padrón-Navarta, J.A., Tommasi, A., Garrido, C.J., López Sánchez-Vizcaíno, V., Gómez-Pugnaire, M.T., Jabaloy, A., Vauchez, A., 2010b. Fluid transfer into the wedge controlled by high-pressure hydrofracturing in the cold top-slab mantle. Earth and Planetary Science Letters, 297(1): 271-286.

Padrón-Navarta, J.A., López Sánchez-Vizcaíno, V., Garrido, C.J., Gómez-Pugnaire, M.T., 2011. Metamorphic record of high-pressure dehydration of antigorite serpentinite to chlorite harzburgite in a subduction setting (Cerro del Almirez, Nevado–Filábride Complex, Southern Spain). Journal of Petrology, 52(10): 2047-2078.

Pan, P., Wood, S.A., 1994. Solubility of Pt and Pd sulfides and Au metal in aqueous bisulfide solutions. Mineralium Deposita, 29(5): 373-390.

Panseri, M., Fontana, E., Tartarotti, P., 2008. Evolution of rodingitic dykes: Metasomatism and metamorphism in the Mount Avic serpentinites (Alpine ophiolites, Southern Aosta Valley). Ofioliti, 33(2): 165-185.

Pearce, J.A., Peate, D.W., 1995. Tectonic implications of the composition of volcanic arc magmas. Annual Review of Earth and Planetary Sciences, 23(1): 251-285.

Pearce, J.A., Stern, R.J., Bloomer, S.H., Fryer, P., 2005. Geochemical mapping of the Mariana arc-basin system: Implications for the nature and distribution of subduction components. Geochemistry, Geophysics, Geosystems, 6(7): Q07006. DOI:10.1029/2004GC000895

Penniston-Dorland, S.C., Walker, R.J., Pitcher, L., Sorensen, S.S., 2012. Mantle–crust interactions in a paleosubduction zone: Evidence from highly siderophile element systematics of eclogite and related rocks. Earth and Planetary Science Letters, 319-320: 295-306.

Penniston-Dorland, S.C., Gorman, J.K., Bebout, G.E., Piccoli, P.M., Walker, R.J., 2014. Reaction rind formation in the Catalina Schist: Deciphering a history of mechanical mixing and metasomatic alteration. Chemical Geology, 384: 47-61.

Penniston-Dorland, S.C., Kohn, M.J., Manning, C.E., 2015. The global range of subduction zone thermal structures from exhumed blueschists and eclogites: Rocks are hotter than models. Earth and Planetary Science Letters, 428: 243-258.

Peucker-Ehrenbrink, B., Bach, W., Hart, S.R., Blusztajn, J.S., Abbruzzese, T., 2003. Rhenium-osmium isotope systematics and platinum group element concentrations in oceanic crust from DSDP/ODP Sites 504 and 417/418. Geochemistry, Geophysics, Geosystems, 4(7): 8911. DOI:10.1029/2002GC000414

Platt, J.P., Anczkiewicz, R., Soto, J.-I., Kelley, S.P., Thirlwall, M., 2006. Early Miocene continental subduction and rapid exhumation in the western Mediterranean. Geology, 34(11): 981-984.

Puga, E., Fanning, M., Díaz de Federico, A., Nieto, J.M., Beccaluva, L., Bianchini, G., Díaz Puga, M.A., 2011. Petrology, geochemistry and U–Pb geochronology of the Betic Ophiolites: Inferences for Pangaea break-up and birth of the westernmost Tethys Ocean. Lithos, 124(3): 255-272.

Puschnig, A.R., 2002. Metasomatic alterations at mafic-ultramafic contacts in Valmalenco (Rhetic Alps, N-Italy). Schweizerische mineralogische und petrographische Mitteilungen, 82(3): 515-536.

Ravizza, G., Blusztajn, J., Prichard, H.M., 2001. Re–Os systematics and platinum-group element distribution in metalliferous sediments from the Troodos ophiolite. Earth and Planetary Science Letters, 188(3-4): 369-381.

Reisberg, L., Rouxel, O., Ludden, J., Staudigel, H., Zimmermann, C., 2008. Re–Os results from ODP Site 801: Evidence for extensive Re uptake during alteration of oceanic crust. Chemical Geology, 248(3-4): 256-271.

Righter, K., Hauri, E.H., 1998. Compatibility of rhenium in garnet during mantle melting and magma genesis. Science, 280(5370): 1737-1741.

Rüpke, L.H., Morgan, J.P., Hort, M., Connolly, J.A.D., 2004. Serpentine and the subduction zone water cycle. Earth and Planetary Science Letters, 223(1-2): 17-34.

Salters, V.J.M., Stracke, A., 2004. Composition of the depleted mantle. Geochemistry, Geophysics, Geosystems, 5(5): Q05004. DOI:10.1029/2003GC000597

Santamaría-López, Á., Sanz de Galdeano, C., 2018. SHRIMP U–Pb detrital zircon dating to check subdivisions in metamorphic complexes: a case of study in the Nevado–Filábride complex (Betic Cordillera, Spain). International Journal of Earth Sciences, 107: 2539-2552.

Scambelluri, M., Rampone, E., 1999. Mg-metasomatism of oceanic gabbros and its control on Ti-clinohumite formation during eclogitization. Contributions to Mineralogy and Petrology, 135(1): 1-17.

Scambelluri, M., Tonarini, S., 2012. Boron isotope evidence for shallow fluid transfer across subduction zones by serpentinized mantle. Geology, 40(10): 907-910.

Scambelluri, M., Bottazzi, P., Trommsdorff, V., Vannucci, R., Hermann, J., Gómez-Pugnaire, M.T., López Sánchez-Vizcaíno, V., 2001. Incompatible element-rich fluids released by antigorite breakdown in deeply subducted mantle. Earth and Planetary Science Letters, 192(3): 457-470.

Scambelluri, M., Pettke, T., Cannaò, E., 2015. Fluid-related inclusions in Alpine high-pressure peridotite reveal trace element recycling during subduction-zone dehydration of serpentinized mantle (Cima di Gagnone, Swiss Alps). Earth and Planetary Science Letters, 429: 45-59.

Schmidt, M.W., Poli, S., 2014. Devolatilization during subduction. In: Holland, H.D., Turekian, K.K. (Eds.), Treatise on Geochemistry, vol. 4. The Crust. Elsevier, pp. 669-701.

Schwarzenbach, E.M., Caddick, M.J., Petroff, M., Gill, B.C., Cooperdock, E.H.G., Barnes, J.D., 2018. Sulphur and carbon cycling in the subduction zone mélange. Scientific Reports, 8(1): 15517. DOI:10.1038/s41598-018-33610-9

Shirey, S.B., Walker, R.J., 1998. The Re-Os isotope system in cosmochemistry and high-temperature geochemistry. Annual Review of Earth and Planetary Sciences, 26(1): 423-500.

Spandler, C., Pirard, C., 2013. Element recycling from subducting slabs to arc crust: A review. Lithos, 170-171: 208-223.

Spandler, C., Hermann, J., Arculus, R., Mavrogenes, J., 2003. Redistribution of trace elements during prograde metamorphism from lawsonite blueschist to eclogite facies; implications for deep subduction-zone processes. Contributions to Mineralogy and Petrology, 146(2): 205-222.

Spandler, C., Hermann, J., Faure, K., Mavrogenes, J.A., Arculus, R.J., 2008. The importance of talc and chlorite "hybrid" rocks for volatile recycling through subduction zones; evidence from the high-pressure subduction mélange of New Caledonia. Contributions to Mineralogy and Petrology, 155(2): 181-198.

Sun, S.-s., McDonough, W.F., 1989. Chemical and isotopic systematics of oceanic basalts: implications for mantle composition and processes. In: Saunders, A.D., Norry, M.J. (Eds.), Magmatism in the Ocean Basins. Geological Society of London Special Publications 42, pp. 313-345.

Sun, W., Bennett, V.C., Eggins, S.M., Kamenetsky, V.S., Arculus, R.J., 2003. Enhanced mantle-to-crust rhenium transfer in undegassed arc magmas. Nature, 422: 294-297.

Syracuse, E.M., van Keken, P.E., Abers, G.A., 2010. The global range of subduction zone thermal models. Physics of the Earth and Planetary Interiors, 183(1-2): 73-90.

Tang, Y., Zhai, Q.-G., Hu, P.-Y., Wang, J., Xiao, X.-C., Wang, H.-T., Tang, S.-H., Lei, M., 2018. Rodingite from the Beila ophiolite in the Bangong–Nujiang suture zone, northern Tibet: New insights into the formation of ophiolite-related rodingite. Lithos, 316-317: 33-47.

Tribuzio, R., Messiga, B., Vannucci, R., Bottazzi, P., 1996. Rare earth element redistribution during high-pressure–low-temperature metamorphism in ophiolitic Fe-gabbros (Liguria, northwestern Italy): implications for light REE mobility in subduction zones. Geology, 24(8): 711-714.

Trommsdorff, V., López Sánchez-Vizcaíno, V., Gómez-Pugnaire, M.T., Müntener, O., 1998. High pressure breakdown of antigorite to spinifex-textured olivine and orthopyroxene, SE Spain. Contributions to Mineralogy and Petrology, 132(2): 139-148.

Ulmer, P., Trommsdorff, V., 1995. Serpentine stability to mantle depths and subduction-related magmatism. Science, 268: 858-861.

van Keken, P.E., Hacker, B.R., Syracuse, E.M., Abers, G.A., 2011. Subduction factory: 4. Depth-dependent flux of H_2O from subducting slabs worldwide. Journal of Geophysical Research: Solid Earth, 116(B1): B01401. DOI:10.1029/2010JB007922

Walker, R.J., Prichard, H.M., Ishiwatari, A., Pimentel, M., 2002. The osmium isotopic composition of convecting upper mantle deduced from ophiolite chromites. Geochimica et Cosmochimica Acta, 66(2): 329-345.

Zack, T., Foley, S.F., Rivers, T., 2002. Equilibrium and disequilibrium trace element partitioning in hydrous eclogites (Trescolmen, Central Alps). Journal of Petrology, 43(10): 1947-1974.

Zanoni, D., Rebay, G., Spalla, M.I., 2016. Ocean floor and subduction record in the Zermatt-Saas rodingites, Valtournenche, Western Alps. Journal of Metamorphic Geology, 34: 941-961.

Declaration of interests

☒ The authors declare that they have no known competing financial interests or personal relationships that could have appeared to influence the work reported in this paper.

☐The authors declare the following financial interests/personal relationships which may be considered as potential competing interests:

Linares,

13 January 2020

Fe oxidation in subducted metarodingites may influence the redox state of slab fluids

Metarodingites release Ca, Mn and Re in fluids from dehydrating serpentinites

Epidote-metarodingites fractionate Sr, Pb, Ba ± Eu from serpentinite-derived fluids

Flux of Re and Ca from metarodingites may metasomatize the sub-arc mantle

Recycling of metarodingites may produce Ca-rich domains in the deep asthenosphere

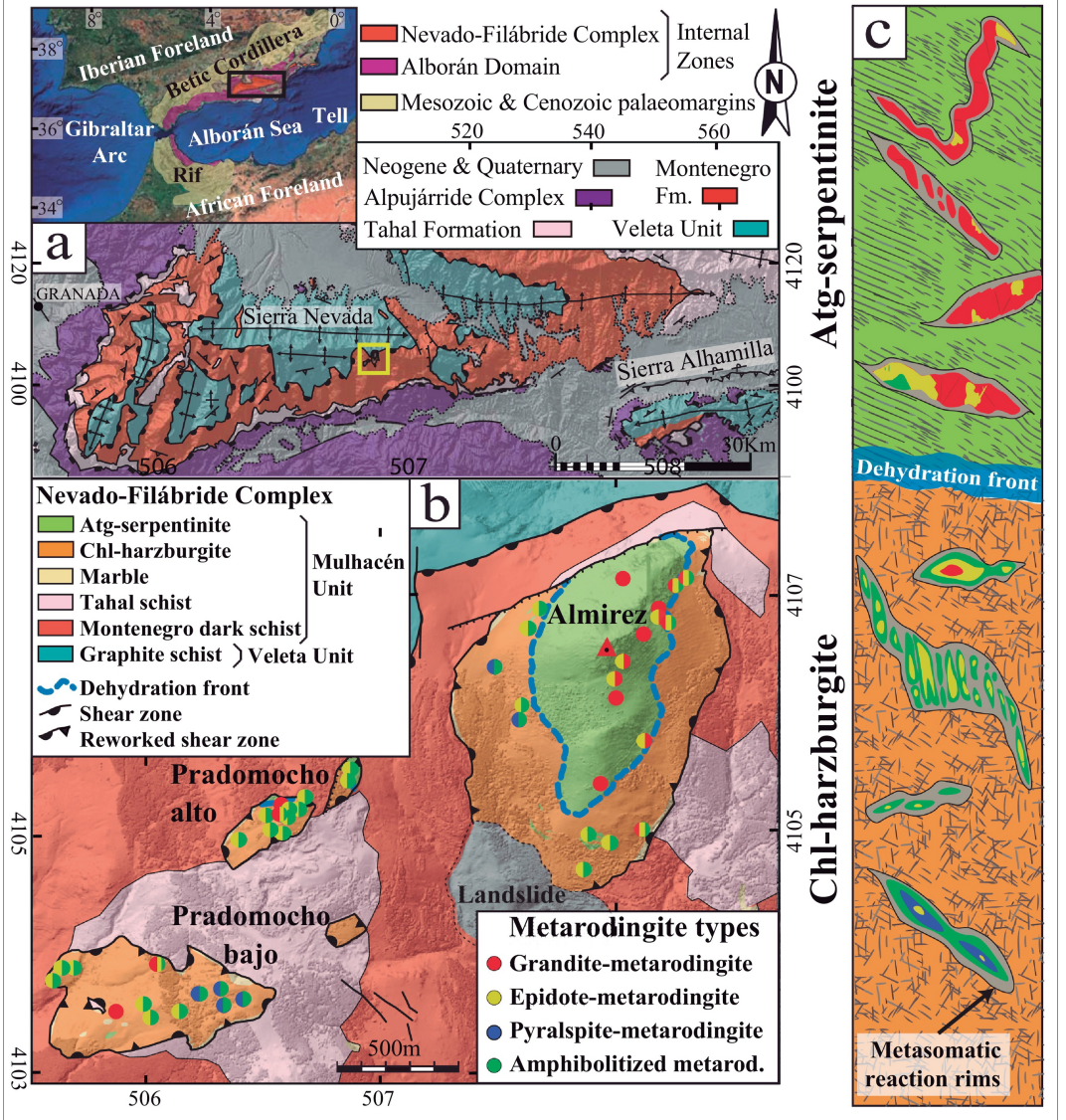
8°
4°
0°
38°
36°
34°
Iberian Foreland
Betic Cordillera
Gibraltar Arc
Alborán Sea
Tell
Rif
African Foreland
Nevado-Filábride Complex
Alborán Domain
Internal Zones
Mesozoic & Cenozoic palaeomargins
520
540
560
N
Neogene & Quaternary
Alpujárride Complex
Tahal Formation
Montenegro Fm.
Veleta Unit
a
GRANADA
Sierra Nevada
Sierra Alhamilla
4120
4100
506
507
508
0
30Km
Nevado-Filábride Complex
Atg-serpentinite
Chl-harzburgite
Marble
Tahal schist
Montenegro dark schist
Graphite schist
Mulhacén Unit
Veleta Unit
Dehydration front
Shear zone
Reworked shear zone
b
Almirez
Pradomocho alto
Pradomocho bajo
Landslide
4107
4105
4103
500m
Metarodingite types
Grandite-metarodingite
Epidote-metarodingite
Pyralspite-metarodingite
Amphibolitized metarod.
c
Atg-serpentinite
Dehydration front
Chl-harzburgite
Metasomatic reaction rims

Figure 1

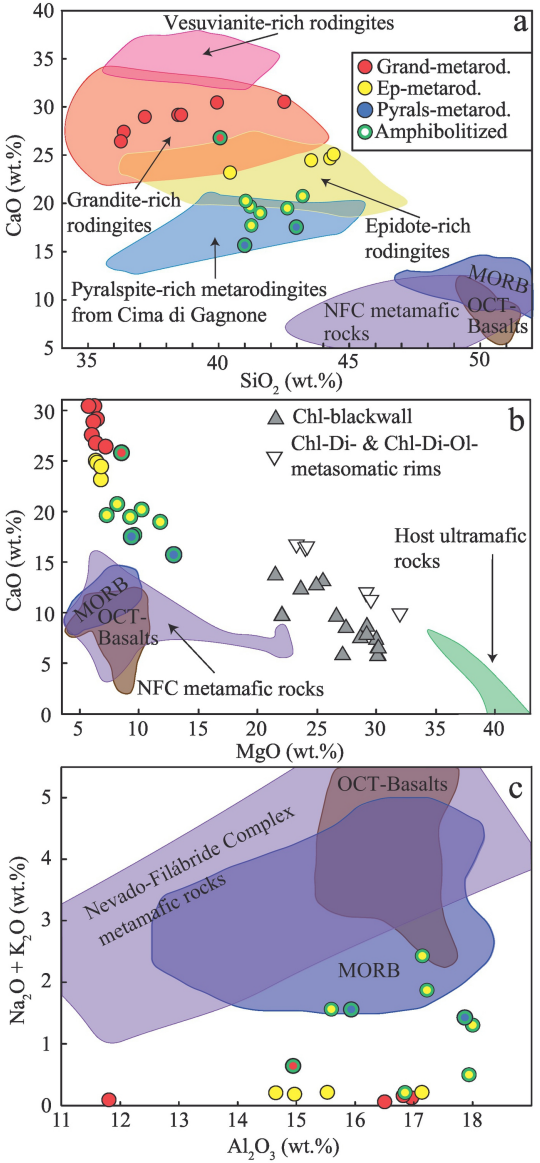
a
Vesuvianite-rich rodingites
Grand-metarod.
Ep-metarod.
Pyrals-metarod.
Amphibolitized
Grandite-rich rodingites
Epidote-rich rodingites
Pyralspite-rich metarodingites from Cima di Gagnone
NFC metamafic rocks
MORB
OCT-Basalts
CaO (wt.%)
SiO2 (wt.%)
b
Chl-blackwall
Chl-Di- & Chl-Di-Ol-metasomatic rims
Host ultramafic rocks
MORB
OCT-Basalts
NFC metamafic rocks
CaO (wt.%)
MgO (wt.%)
c
OCT-Basalts
Nevado-Filábride Complex metamafic rocks
MORB
Na2O + K2O (wt.%)
Al2O3 (wt.%)

Figure 2

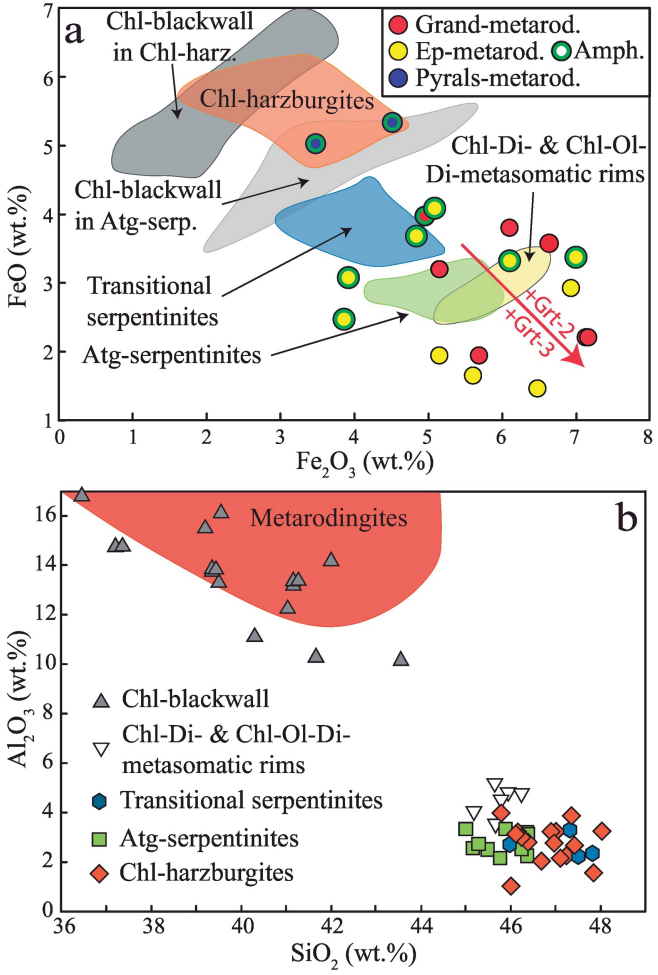
a
Chl-blackwall in Chl-harz.
Chl-harzburgites
Chl-blackwall in Atg-serp.
Transitional serpentinites
Atg-serpentinites
Chl-Di- & Chl-Ol-Di-metasomatic rims
+Grt-2
+Grt-3
Grand-metarod.
Ep-metarod.
Amph.
Pyrals-metarod.
FeO (wt.%)
Fe2O3 (wt.%)
b
Metarodingites
Chl-blackwall
Chl-Di- & Chl-Ol-Di-metasomatic rims
Transitional serpentinites
Atg-serpentinites
Chl-harzburgites
Al2O3 (wt.%)
SiO2 (wt.%)

Figure 3

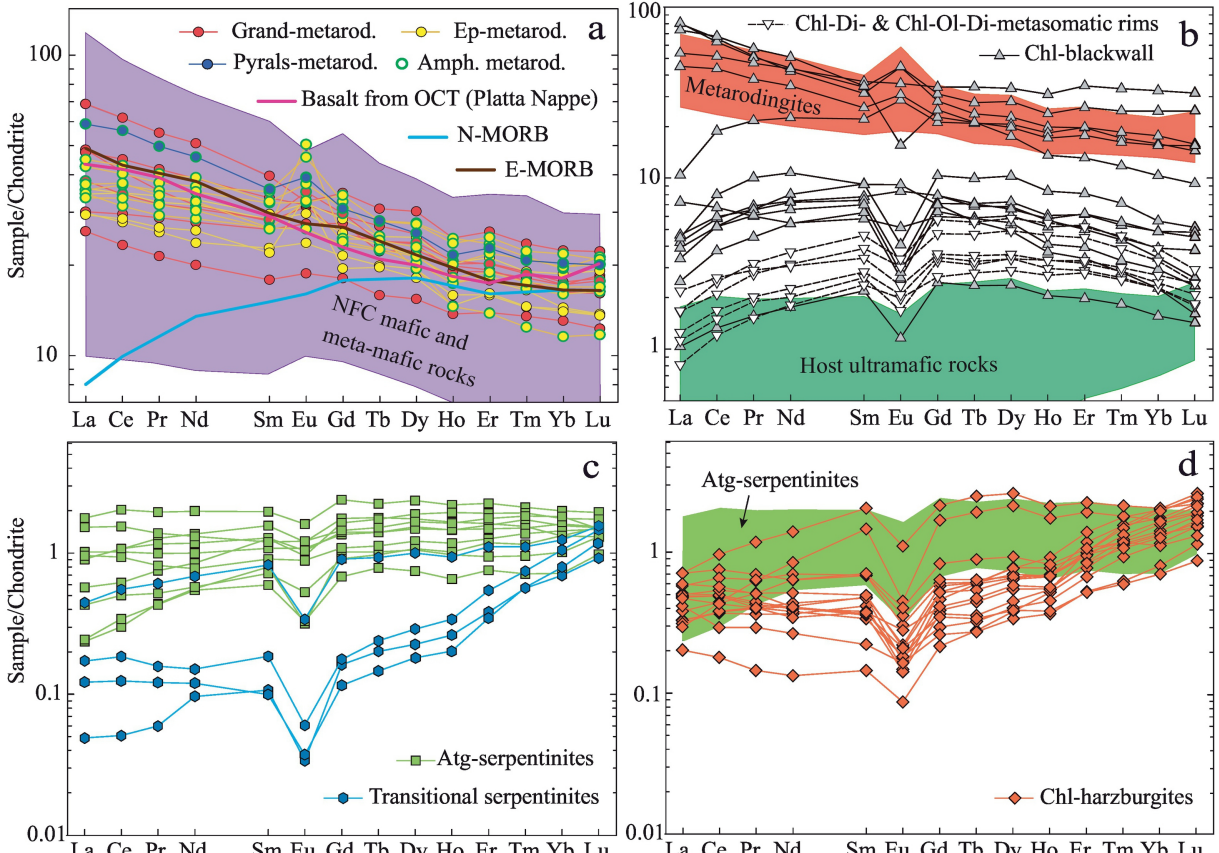
a
Grand-metarod.
Ep-metarod.
Pyrals-metarod.
Amph. metarod.
Basalt from OCT (Platta Nappe)
N-MORB
E-MORB
NFC mafic and
meta-mafic rocks
Sample/Chondrite
100
10
La Ce Pr Nd Sm Eu Gd Tb Dy Ho Er Tm Yb Lu
b
Chl-Di- & Chl-Ol-Di-metasomatic rims
Chl-blackwall
Metarodingites
Host ultramafic rocks
100
10
1
La Ce Pr Nd Sm Eu Gd Tb Dy Ho Er Tm Yb Lu
c
Sample/Chondrite
1
0.1
0.01
Atg-serpentinites
Transitional serpentinites
La Ce Pr Nd Sm Eu Gd Tb Dy Ho Er Tm Yb Lu
d
Atg-serpentinites
1
0.1
0.01
Chl-harzburgites
La Ce Pr Nd Sm Eu Gd Tb Dy Ho Er Tm Yb Lu

Figure 4

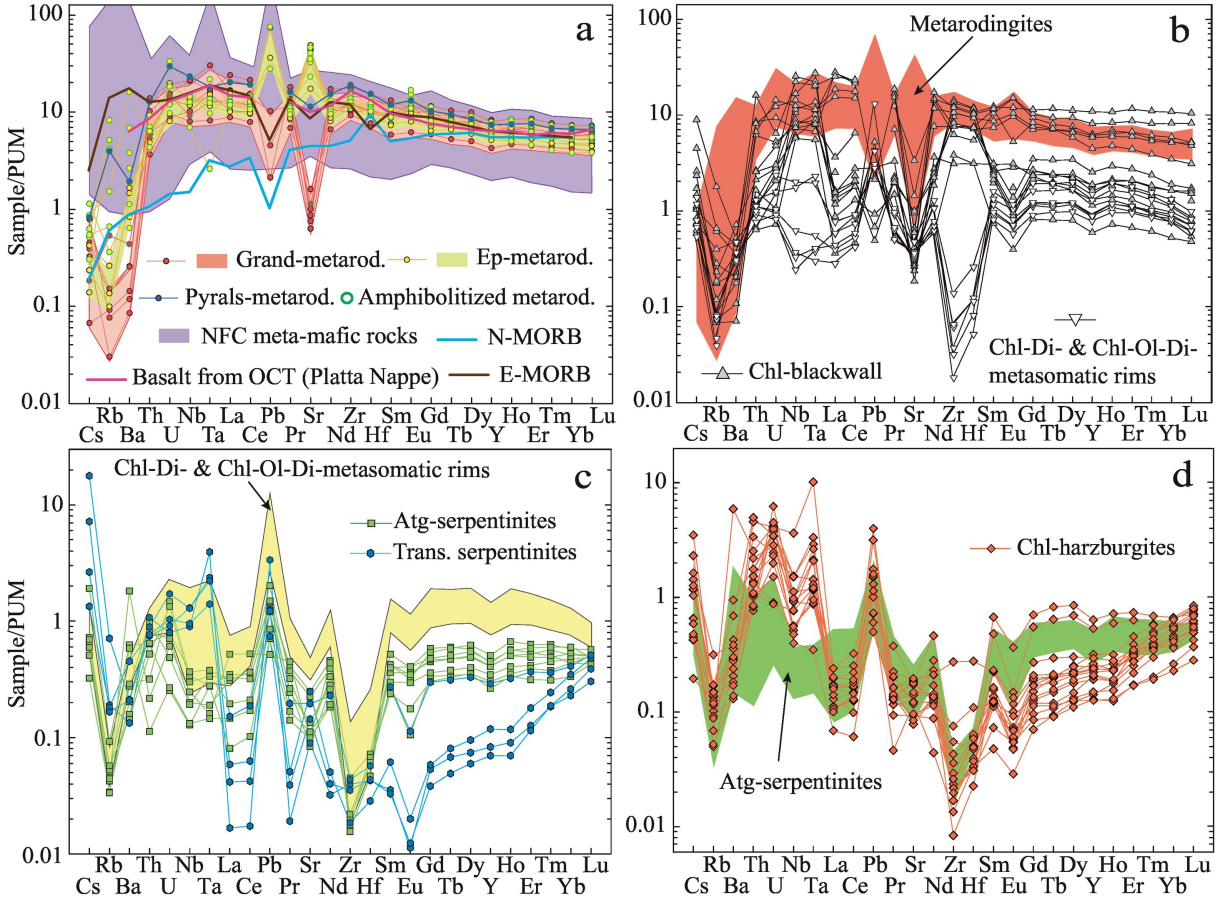
a
Sample/PUM
Grand-metarod.
Ep-metarod.
Pyrals-metarod.
Amphibolitized metarod.
NFC meta-mafic rocks
N-MORB
Basalt from OCT (Platta Nappe)
E-MORB
b
Metarodingites
Chl-blackwall
Chl-Di- & Chl-Ol-Di-metasomatic rims
c
Chl-Di- & Chl-Ol-Di-metasomatic rims
Atg-serpentinites
Trans. serpentinites
d
Chl-harzburgites
Atg-serpentinites
Rb Th Nb La Pb Sr Zr Sm Gd Dy Ho Tm Lu
Cs Ba U Ta Ce Pr Nd Hf Eu Tb Y Er Yb

Figure 5

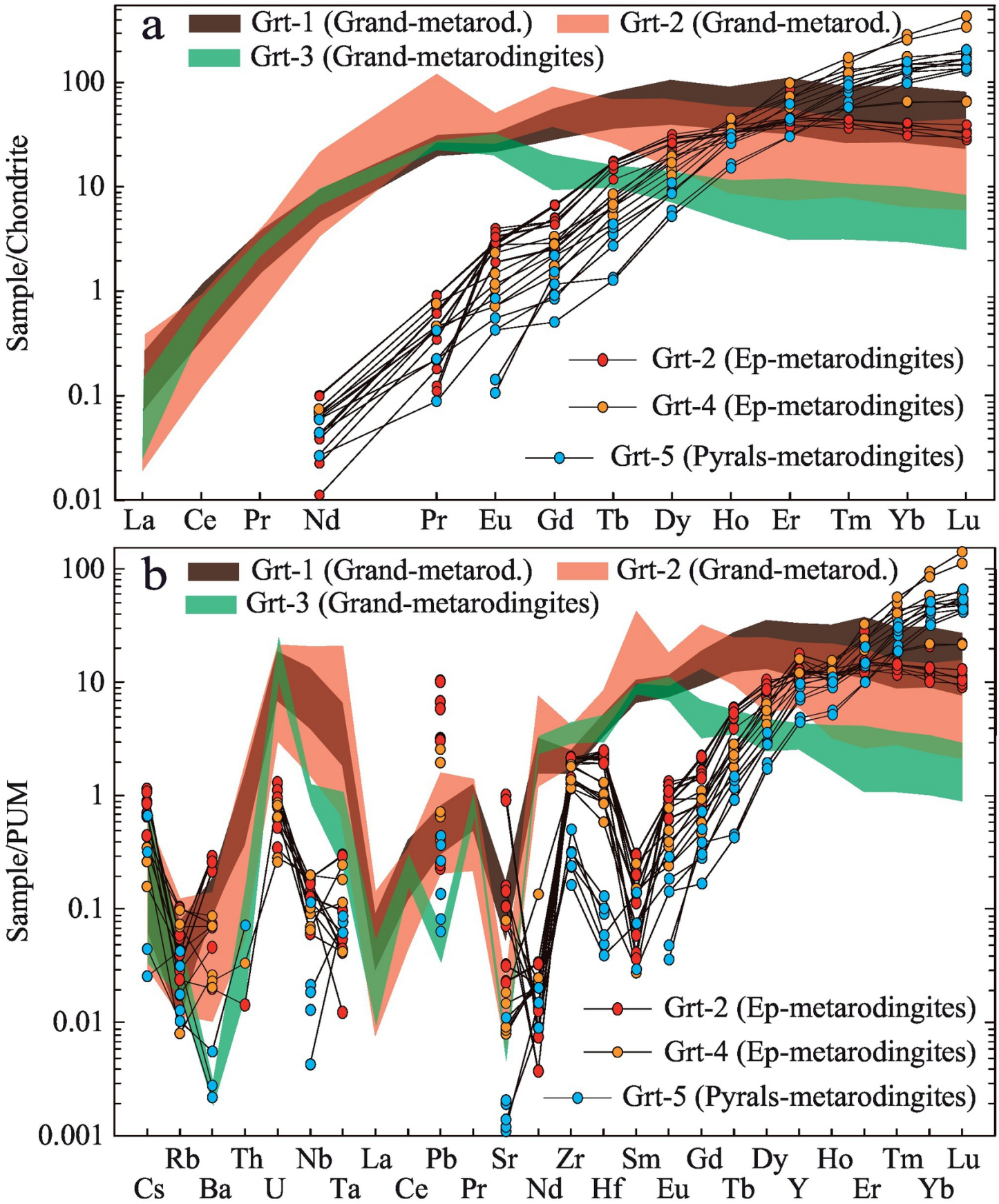
a
Grt-1 (Grand-metarod.)
Grt-2 (Grand-metarod.)
Grt-3 (Grand-metarodingites)
Sample/Chondrite
100
10
1
0.1
0.01
Grt-2 (Ep-metarodingites)
Grt-4 (Ep-metarodingites)
Grt-5 (Pyrals-metarodingites)
La Ce Pr Nd Pr Eu Gd Tb Dy Ho Er Tm Yb Lu
b
Grt-1 (Grand-metarod.)
Grt-2 (Grand-metarod.)
Grt-3 (Grand-metarodingites)
Sample/PUM
100
10
1
0.1
0.01
0.001
Grt-2 (Ep-metarodingites)
Grt-4 (Ep-metarodingites)
Grt-5 (Pyrals-metarodingites)
Rb Th Nb La Pb Sr Zr Sm Gd Dy Ho Tm Lu
Cs Ba U Ta Ce Pr Nd Hf Eu Tb Y Er Yb

Figure 6

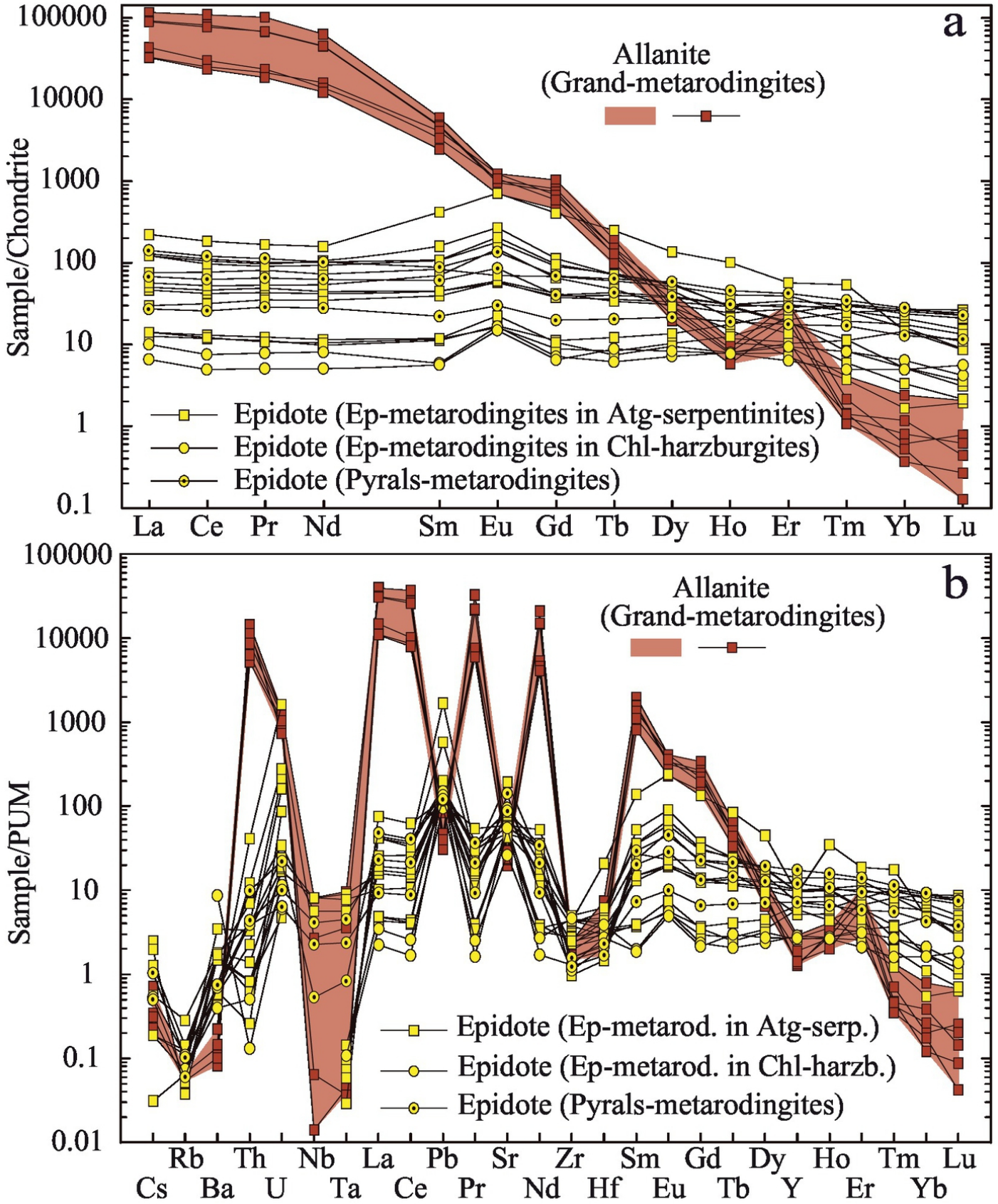
a
Allanite
(Grand-metarodingites)
Epidote (Ep-metarodingites in Atg-serpentinites)
Epidote (Ep-metarodingites in Chl-harzburgites)
Epidote (Pyrals-metarodingites)
Sample/Chondrite
100000
10000
1000
100
10
1
0.1
La Ce Pr Nd Sm Eu Gd Tb Dy Ho Er Tm Yb Lu
b
Allanite
(Grand-metarodingites)
Epidote (Ep-metarod. in Atg-serp.)
Epidote (Ep-metarod. in Chl-harzb.)
Epidote (Pyrals-metarodingites)
Sample/PUM
100000
10000
1000
100
10
1
0.1
0.01
Cs Rb Ba Th U Nb Ta La Ce Pb Pr Sr Nd Zr Hf Sm Eu Gd Tb Dy Y Ho Er Tm Yb Lu

Figure 7

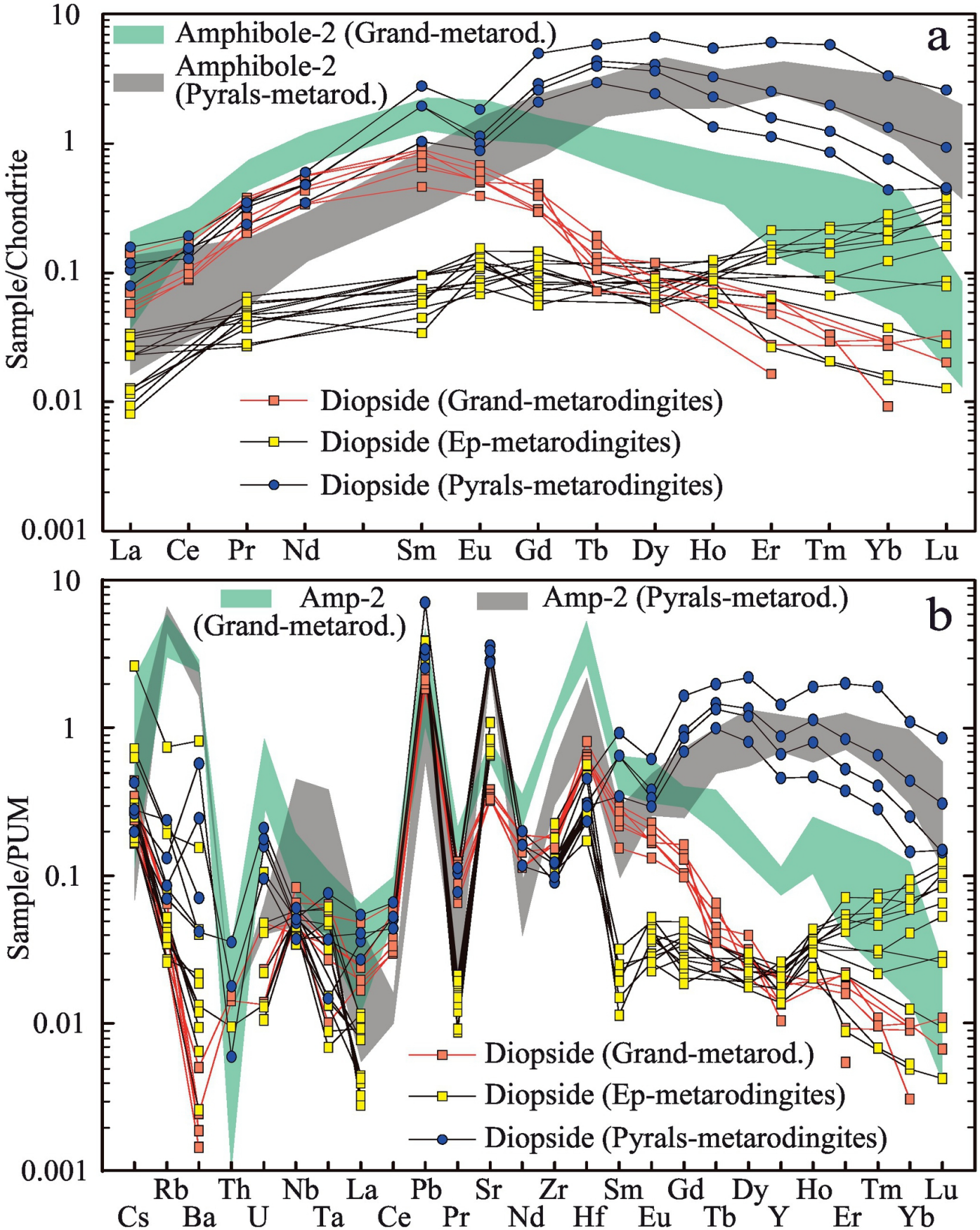
a
Amphibole-2 (Grand-metarod.)
Amphibole-2
(Pyrals-metarod.)
Diopside (Grand-metarodingites)
Diopside (Ep-metarodingites)
Diopside (Pyrals-metarodingites)
Sample/Chondrite
10
1
0.1
0.01
0.001
La Ce Pr Nd Sm Eu Gd Tb Dy Ho Er Tm Yb Lu
b
Amp-2
(Grand-metarod.)
Amp-2 (Pyrals-metarod.)
Diopside (Grand-metarod.)
Diopside (Ep-metarodingites)
Diopside (Pyrals-metarodingites)
Sample/PUM
10
1
0.1
0.01
0.001
Cs Rb Ba Th U Nb Ta La Ce Pb Pr Sr Nd Zr Hf Sm Eu Gd Tb Dy Y Ho Er Tm Yb Lu

Figure 8

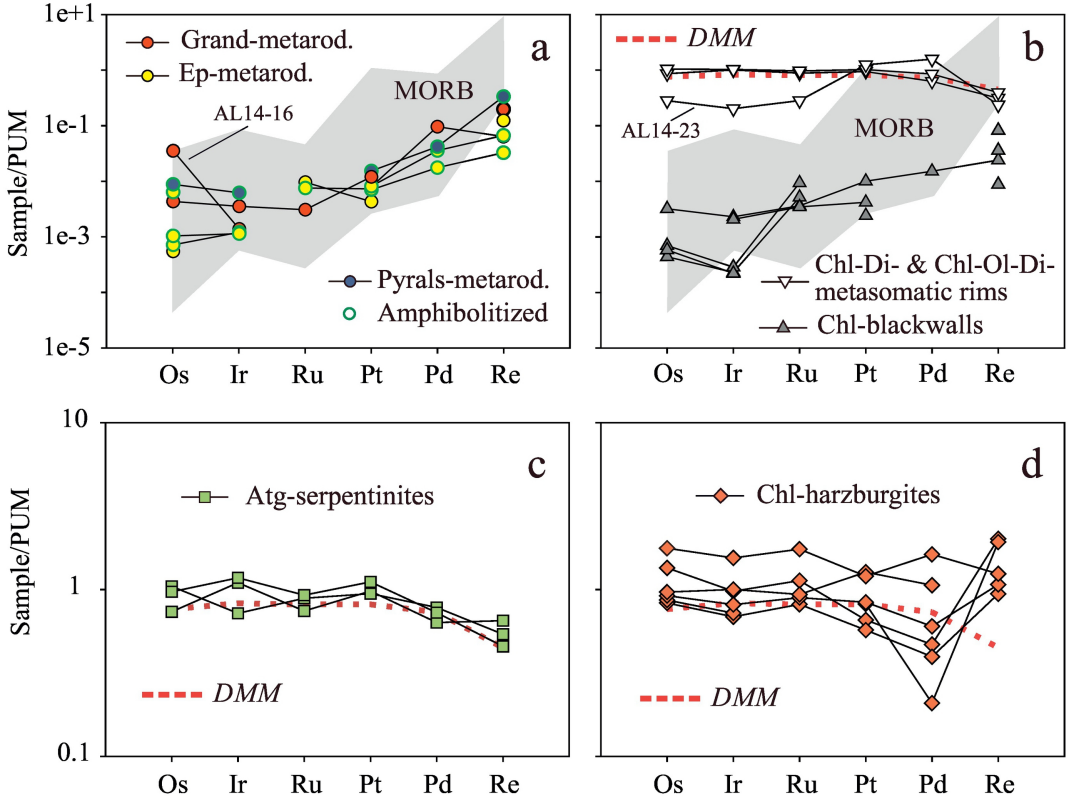
a
Grand-metarod.
Ep-metarod.
AL14-16
MORB
Pyrals-metarod.
Amphibolitized
Sample/PUM
1e+1
1e-1
1e-3
1e-5
Os
Ir
Ru
Pt
Pd
Re
b
DMM
AL14-23
MORB
Chl-Di- & Chl-Ol-Di-metasomatic rims
Chl-blackwalls
c
Atg-serpentinites
DMM
10
1
0.1
d
Chl-harzburgites
DMM

Figure 9

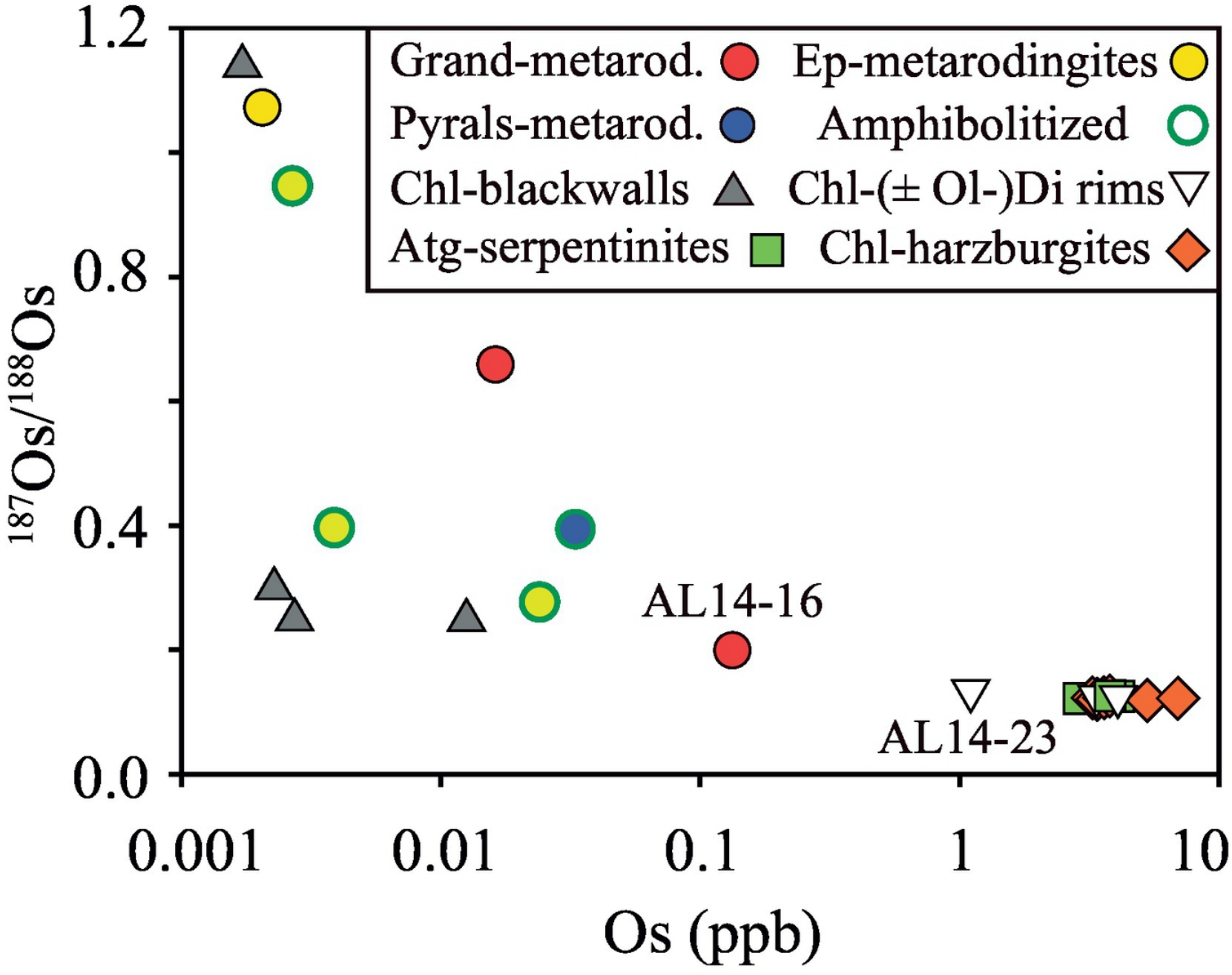
Grand-metarod.
Ep-metarodingites
Pyrals-metarod.
Amphibolitized
Chl-blackwalls
Chl-(± Ol-)Di rims
Atg-serpentinites
Chl-harzburgites
AL14-16
AL14-23
1.2
0.8
0.4
0.0
0.001
0.01
0.1
1
10
$^{187}Os/^{188}Os$
Os (ppb)

Figure 10

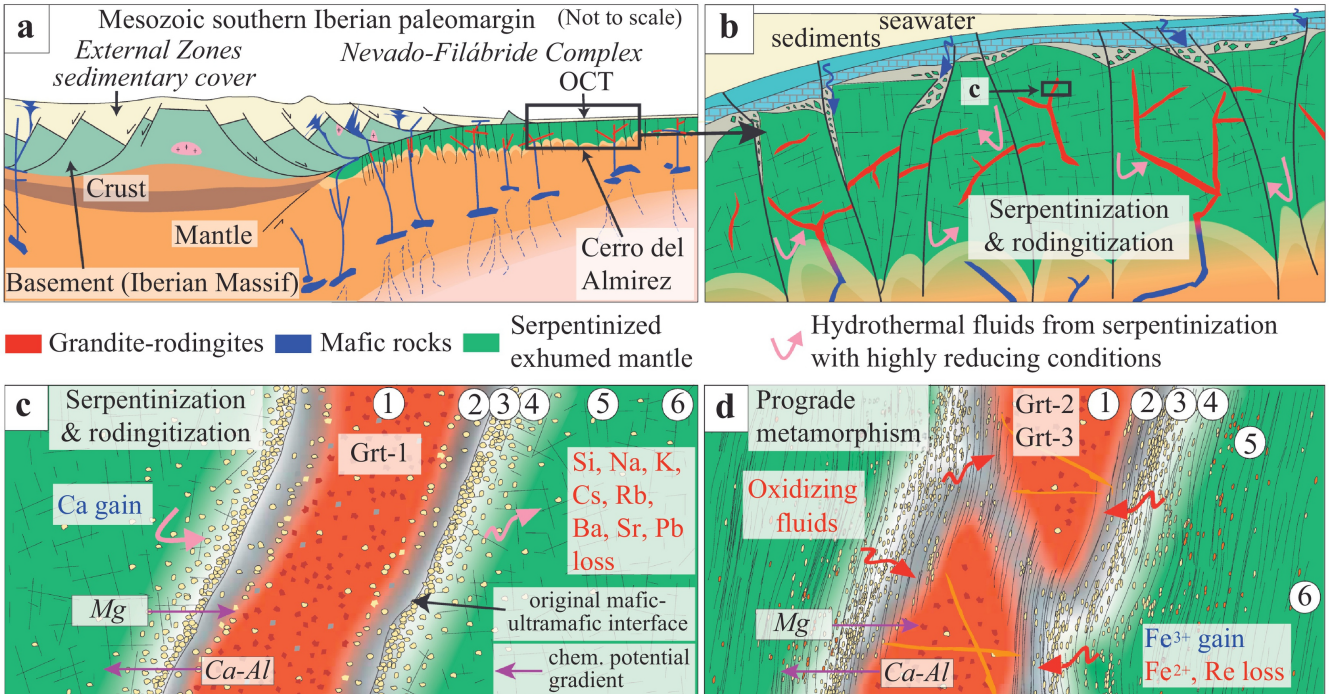

(1) Grandite-(meta)rodingite, (2) Chl-blackwall, (3) Chl-Di-metasomatic rim, (4) Chl-Ol-Di-metasomatic rim, (5) Serpentinite Close, (6) Serpentinite Far

Figure 11